



ROOM TEMPERATURE SPIN ENSEMBLES FOR PRECISION MEASUREMENTS

Experimental development of room temperature atomic spin ensembles for quantum sensing by improving magnetic field environment and optimizing geometry

Written by *Ryan Yde*
August 17, 2020

Supervised by
Eugene Polzik, Professor, NBI
Michael Zugenmaier, Postdoc, NBI



NAME OF INSTITUTE: Niels Bohr Institute

NAME OF DEPARTMENT: QUANTOP

AUTHOR(S): Ryan Yde

EMAIL: knb392@alumni.ku.dk

TITLE AND SUBTITLE: Room temperature spin ensembles for precision measurements
- Experimental development of room temperature atomic spin ensembles for quantum sensing by improving magnetic field environment and optimizing geometry

SUPERVISOR(S): Eugene Polzik, Professor, NBI
Michael Zugenmaier, Postdoc, NBI

HANDED IN: 08.17.2020

DEFENDED:

NAME _____

SIGNATURE _____

DATE _____

Abstract

Atomic vapor cells with anti-relaxation coating have been used successfully for back-action evading measurements [21] and are promising candidates for improving gravitational wave detection. An important parameter is the optical depth, thus long vapor cells are preferable. In order to reach long coherence times, vapor cells require homogeneous magnetic fields over the length of the entire cell, which can be achieved by printed circuit board (PCB) coils. We present the theory behind and design of a system of PCB-coils. By applying the method of magneto-optical resonance spectroscopy (MORS) to an atomic vapor cell we characterize the produced magnetic profiles and optimize the coil configuration. We obtain a magnetic homogeneity with a relative standard deviation of 1.1‰ over 8 cm. Using a $5 \times 5 \times 80 \text{ mm}^3$ vapor cell, subjected to our produced magnetic environment, we obtain a MORS-signal with a linewidth as low as $(7.7 \pm 0.5) \text{ Hz}$ at a Larmor frequency of 433 Hz. We observe atomic spin noise and present a preliminary investigation of the change with magnetic fields and light power.

Contents

1	Introduction	4
2	Theoretical Foundation	6
2.1	Gravitational Waves	6
2.2	Cesium	10
2.2.1	Atomic Structure of Cesium	10
2.2.2	Quantum Defect	10
2.2.3	Fine Structure	11
2.2.4	Hyperfine Structure	11
2.2.5	Zeeman Splitting	12
2.3	Atomic Spin Ensembles	14
2.4	Optical Pumping	15
2.4.1	Selection Rules	15
2.4.2	Optical Pumping Scheme	16
2.5	MORS	18
2.5.1	Larmor Precession	18
2.5.2	Magnetic Dipole Transitions	19
2.5.3	Polarization of Light	20
2.5.4	Faraday Interaction	21
2.5.5	Traditional MORS	21
2.5.6	Colinear MORS	23
2.5.7	Vapor Cells	23
2.5.8	Magnetic Environment	24
3	Magnetic Field Generation	26
3.1	PCB Design	26
3.2	Mathematical Basis	29
3.3	Programmatic Implementation	31
4	Coil Characterization	34
4.1	Assembly	34
4.2	Cell Measurements - Outside Shield	34
4.3	Cell Measurements - Inside Shield	38
4.4	Optimizing Coil Design	42
4.4.1	The Probe	42
4.4.2	Outside Shield	42
4.4.3	Inside Shield	44
4.4.4	Degaussing	46
4.5	Bio-Shield Coil Characterization	48
4.5.1	Bias Coils	48
4.5.2	Compensation Coils	51

5	Long Cell Measurements	54
5.1	Y-Coils	55
5.2	Z-Coils	58
6	Noise Measurements	61
6.1	Different Larmor Frequencies	63
6.2	Changing Probe Power	65
7	Discussion	68
7.1	Conclusion	68
7.2	Outlook	68
7.3	Acknowledgments	70
	Appendices	73

1 Introduction

For centuries physics and engineering have contributed to an ever increasing body of knowledge and understanding of the universe. On all scales, devices are built to push the limits of what is possible to observe. Whereas a classroom microscope enables us to explore the world in a regime otherwise too small to capture, it is however still within the spectrum, observable to the human eye. Other devices are extensions to the human sensory system. An infrared camera detects frequencies slightly outside the visible part of the electromagnetic spectrum, while a radio responds to much lower frequencies.

In this regard, one of the most astounding endeavors undertaken in modern times, is the development and construction of gravitational wave observatories like LIGO. These spectacular structures have opened the doors to a hitherto unexplored regime of research in fields like cosmology and astrophysics. As is the case for all types of measuring devices, gravitational wave detectors (GWDs) have a limit to their level of sensitivity.

GWDs are essentially giant interferometers. A laser beam is split into two beams, traveling through two different vacuum tubes at the end of which, mirrors are located. The beams are then reflected, and if the arms have equal lengths, the two beams interfere destructively and no signal is detected. Depending on its polarization and axis of propagation, a passing gravitational wave may affect the lengths of the two arms differently, resulting in a signal.

Sensitivity is compromised by noise, and in GWDs mechanical noise has been decreased to a level where quantum fluctuations become significant. In laser beams, the fluctuations in photon number, called shot noise, effectively decrease with increasing power. For this reason, LIGO uses intra cavity laser powers up to ~ 1 MW [4]. Operating at such high powers does however come with a price. When photons are reflected, momentum is transferred to the mirrors resulting in an uncertainty in their positions, and this uncertainty is projected back onto the light - a phenomenon known as quantum back action (QBA). At the ideal laser power, the noise due to a combination of shot noise and QBA reaches its minimum, known as the standard quantum limit (SQL) [22].

In [18, 29] a method is proposed on how to overcome this SQL in GWDs by using a spin system with a negative effective mass. This includes two entangled light beams, one of which would travel to LIGO while the other travels to the spin system. In the process of quantum state preparation of such spin systems, the magnetic environment plays a vital role. The magnetic field needs to be both stable in time and homogeneous in space. The optimization of such a magnetic environment has been the main focus of this thesis.

The spin system we use is a glass cell containing vaporized cesium atoms. We design a coil system with the aim of optimizing the homogeneity of the magnetic field to which the vapor cell is subjected, in order to have a well defined and long-lived collective spin state. The state of the system is then read by means of optical magnetometry.

In chapter 2 we begin with a brief review of the theory that predicted the existence of gravitational waves. We then describe the atomic structure and energy levels of cesium. We present the mechanisms behind optical pumping schemes, and describe the MORS measurement method.

In chapter 3 we focus on the theory behind, and design of, the coil system used to produce magnetic fields, and comment on the programmatic and computational aspects of the process.

In chapter 4 we characterize the magnetic profiles of the designed coils. We optimize the coil configuration and present the process of improving magnetic shielding.

In chapter 5 we modify the experimental setup by mounting an 8 cm vapor cell inside the coil system, and test the performance of the complete configuration.

In chapter 6 we switch gears, and probe the atomic spin ensemble with light, exploring some of the noise contributions.

Finally we devote chapter 7 to a discussion of the achieved results and present a few ideas on future improvements.

2 Theoretical Foundation

We begin this section with a justification of the extensive efforts that have been put into the pursuit of enabling the detection of gravitational waves. We then proceed to present the theory behind optical magnetometry. We explain the atomic structure of cesium and consider how the different quantum states give rise to different energy levels, under certain conditions like the effect from externally applied magnetic fields. We describe the process of atomic transitions and the mechanisms behind optical pumping schemes. Different polarization states of light are reviewed together with some aspects of atom-light interaction. We then describe the measuring method known as MORS which has been used in several of the experiments presented in this thesis. Finally we consider some of the characteristics of vapor cells in general.

2.1 Gravitational Waves

Over the past 40 years the US National Science Foundation has spent more than a billion dollars on the development and construction of LIGO [5]. With a budget of such magnitude, leading scientists in this endeavor must presumably have had a high level of certainty in the existence of gravitational waves. It thus seems appropriate to begin this thesis with a brief insight to the theory that gave birth to the idea of gravitational waves.

Before Einstein it was commonly accepted among physicists that space and time were separated. However, through his formulation of the theory of relativity, Einstein realized the flaw in this assumption - they are wound together, forming a fabric called space-time. Whereas electromagnetic waves propagate *through* space-time, gravitational waves are ripples in the fabric of space-time itself.

Coordinates in relativity are called *events* and they have both time and space components. We write a four-dimensional coordinate x as

$$x = (x^0, x^1, x^2, x^3) \tag{1}$$

where $x^0 = t$ is the time-coordinate ¹, and x^i is the spatial coordinates with $i \in [1, 2, 3]$. Note here that x^i is a notation and not exponentials, e.g. x^2 is not x squared. The theory of relativity came in two steps - *special* relativity (SR) and *general* relativity (GR). A common misconception is that SR does not account for accelerations. The truth is that SR does not account for gravity and in relativity gravity and geometry go hand in hand. Thus SR describes a flat space-time, analogous to a flat Euclidean space, called Minkowski space. The geometry of space-time is defined by the metric $g_{\mu\nu}$ and in relativity the metric defines the invariant line-element ds as

¹Strictly speaking this should be the *proper* time τ , but in the spirit of simplicity we assume $t = \tau$.

$$\begin{aligned}
ds^2 &= \sum_{\mu=0}^3 \sum_{\nu=0}^3 g_{\mu\nu} dx^\mu dx^\nu \\
&= g_{\mu\nu} dx^\mu dx^\nu
\end{aligned} \tag{2}$$

where we have introduced Einstein-notation meaning that whenever an index appears both up and down it implies that we sum over that index.

In Minkowski space the metric $g = \eta$ is given by

$$\eta = \begin{pmatrix} -1 & 0 & 0 & 0 \\ 0 & 1 & 0 & 0 \\ 0 & 0 & 1 & 0 \\ 0 & 0 & 0 & 1 \end{pmatrix} \tag{3}$$

The line-element in eq.2 thus becomes

$$ds^2 = -dt^2 + (dx^1)^2 + (dx^2)^2 + (dx^3)^2. \tag{4}$$

Ignoring the time-coordinate we see that eq.4 reduces to the Pythagorean theorem. Thus, the lower right 3×3 matrix in eq.3 describes a flat Euclidean space which means that no gravity is present.

The idea now is to add a small amount of gravity and examine the effect on the line-element. We write

$$g_{\mu\nu}(x) = \eta_{\mu\nu} + h_{\mu\nu}(x) \tag{5}$$

where $h_{\mu\nu}(x)$ is the contribution to the metric by gravity. In the weak field limit we require $|h_{\mu\nu}(x)| \ll 1$. Make now the ansatz

$$h_{\mu\nu}(x) = A_{\mu\nu} e^{ik_\rho x^\rho} \tag{6}$$

where $A_{\mu\nu}$ is a constant and k^μ is the 4-dimensional wave vector. It can be shown² that eq.6 corresponds to a monochromatic plane wave propagating with $v = c$, i.e. at the speed of light. This is a rather remarkable result which emerges when studying the theory of relativity in the limit of weak gravitational fields - hence the name, gravitational waves. The effect of these gravitational waves on the fabric of space-time gives rise to some particularly interesting phenomena which are vital in the detection of such waves.

To illustrate this, let us explore the relative motion between two test-particles A and B each following

$$x^0 = t \quad , \quad x^i = \text{const.} \tag{7}$$

²A more detailed derivation of this can be found in appendix C.

meaning that we place them in spatial coordinates and let them stay there, i.e. only the time-coordinate changes. Assuming k^μ to propagate along x^3 we place them in the (x^1, x^2) -plane as

$$\begin{aligned} x_A &= (x_A^1, x_A^2, x_A^3) \\ x_B &= (x_A^1 + L_0 \cos \theta, x_A^2 + L_0 \sin \theta, x_A^3). \end{aligned} \quad (8)$$

An illustration is seen in fig.1.

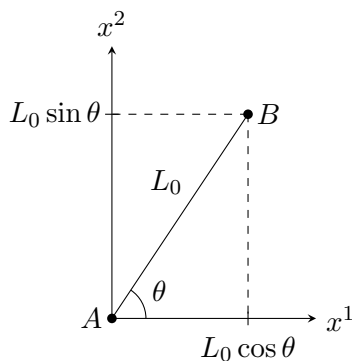


Figure 1: An illustration of the positions of the two test-particles A and B .

As shown in appendix C, the line-element in eq.2 can be written

$$ds^2 = -dt^2 + (1 + h_{11})(dx^1)^2 + 2h_{12}dx^1dx^2 + (1 - h_{11})(dx^2)^2 + (dx^3)^2. \quad (9)$$

By integrating eq.9 along the line connecting particles A and B , we can find an expression of the length $L(t)$ between the two particles

$$L(t) = \left[1 + \frac{1}{2}h_{11}(t) \cos(2\theta) + \frac{1}{2}h_{12}(t) \sin(2\theta) \right] L_0. \quad (10)$$

We see that the length L is time-dependent through $h_{\mu\nu}$. It is this relative motion of test-particles that makes it possible to detect gravitational waves. Note that since $\cos(2\theta) = \sin(2(\theta + \pi/4))$, the effect on L from h_{11} compared to that of h_{12} is rotated 45 degrees. Hence they are linearly independent. In reality, the length $L(t)$ is measured by lasers. Since it takes time for the light to travel to and from a particle (or mirror), the change in length must happen slowly compared to the travel time of light. In other words, the size of the detector should be much smaller than the wavelength of the gravitational wave

$$L_0 \ll \lambda. \quad (11)$$

In gravitational wave detection schemes, light interferometers like LIGO are used to detect high frequency gravitational fields with a frequency in the order of ~ 100 Hz. For a

wave traveling at the speed of light, this corresponds to $\lambda \approx 3000$ km and with the arms of LIGO being 4 kilometers, eq.11 is fulfilled.

To further clarify the effect exploited by GWDs, let us examine a grid of test-particles in the (x^1, x^2) -plane. We may simplify eq.10 to get

$$L(t) \propto L_0 [\cos(\omega t) \cos(2\theta)]. \quad (12)$$

For two particles lying along x^1 where $\theta = 0$ we have $\cos(2\theta) = 1$. For another pair of particles, lying along x^2 where $\theta = \pi/2$, we get $\cos(2\theta) = -1$. This means that the lengths between these two pairs of particles respectively oscillate out of phase. An illustration of this is seen in fig.2. When space-time is stretched along x^1 it is compressed along x^2 and vice versa. When this happens to the arms of a GWD it enables the detection of gravitational waves.

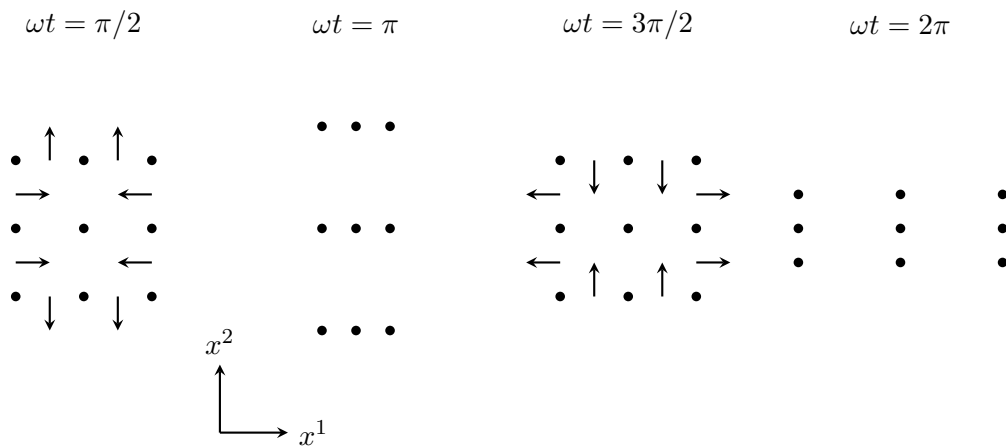


Figure 2: An illustration of the strain and tension of space-time due to a gravitational wave with frequency ω propagating along x^3 .

2.2 Cesium

We now turn the attention from astronomical to atomic scales. Our setup is centered around a glass cell containing cesium atoms like the one seen in fig.3 Inside the stem is a droplet of solid cesium and at room temperature a certain fraction of these atoms vaporize and diffuse to the hollow cubic part of the cell.



Figure 3: An example of a 5 mm cubic vapor cell [9].

2.2.1 Atomic Structure of Cesium

The strength of a given light-atom interaction is determined partly by the atomic structure of the atom in question. In our experiments we use cesium which has only one stable isotope, the cesium-133 with electron configuration [8]

$$1s^2 2s^2 p^6 3s^2 p^6 d^{10} 4s^2 p^6 d^{10} 5s^2 p^6 6s^1 = [\text{Xe}]6s^1 \quad (13)$$

here written in the commonly used nl^x -notation where n is the *principle quantum number*, l the *orbital angular momentum quantum number*, x the number of electrons in that state and $\{s, p, d, f\}$ represents $l = \{1, 2, 3, 4\}$. As seen by the right hand side of eq.13 this configuration corresponds to the noble gas xenon with a valence electron added in the 6s-state, constituting the ground state of the cesium atom.

2.2.2 Quantum Defect

In hydrogen the energy of an electron depends only on its principle quantum number and in effect the energies of 3s, 3p and 3d configurations are degenerate. In atoms with more than one electron however this degeneracy is lifted and we will now briefly investigate why. Cesium, having only one valence electron, is an alkali metal which are often called *hydrogen-like*. This is due to the fact that when considering a valence electron, i.e. an electron in the outermost shell, the repulsion from electrons in the inner shells can be combined with the attraction of the protons in the nucleus and approximated as a single central potential - just like in hydrogen. This is called the *central-field approximation* and it works as long as the electron in question has much bigger distance to the nucleus than the inner-shell electrons. Now, the radial part of electron wave functions in alkali

metals have similar shape to those of hydrogen, and s-orbitals have higher probabilities for being closer to the nucleus than p- or d-orbitals [10] and thus energies are non-degenerate for these orbitals. An example of this effect on cesium atoms is visualized in fig.4.

2.2.3 Fine Structure

Another feature that affects the energy levels of atoms is the *spin-orbit* interaction or *fine structure* - in our specific case of the valence electron in eq.13.

Electrons have intrinsic magnetic moment $\boldsymbol{\mu} = -g_S\mu_B\mathbf{S}$, where g_S is the g-factor, μ_B the Bohr magneton and \mathbf{S} the electron spin. In addition to intrinsic spin the electron also has an orbital angular momentum \mathbf{L} and since a charge moving in an electric potential produces a magnetic field \mathbf{B} , the magnetic moment interacts with this produced field through the Hamiltonian [10]

$$\begin{aligned} H &= -\boldsymbol{\mu} \cdot \mathbf{B} \\ &\propto \mathbf{S} \cdot \mathbf{L}. \end{aligned} \tag{14}$$

s-orbitals have $L = 0$ and are thus not affected by spin-orbit interaction whereas p- and d-orbitals, having $L \neq 0$ are. Combining Pauli's exclusion principle, which states that two electrons cannot simultaneously occupy states with identical sets of quantum numbers, with the introduction of the *total angular momentum* $\mathbf{J} = \mathbf{L} + \mathbf{S}$, splits the first excited state of a cesium atom, the 6p-state, into two fine-structure sublevels with

$$|\mathbf{J}| = J = L \pm S = 1 \pm \frac{1}{2} = \left\{ \frac{1}{2}, \frac{3}{2} \right\}. \tag{15}$$

In the literature these are commonly written in the form $^{2s+1}L_j$ giving $^2P_{1/2}$ and $^2P_{3/2}$ - see fig.4 for an illustration.

2.2.4 Hyperfine Structure

Similar to electrons, the nucleus of an atom also has a magnetic moment $\boldsymbol{\mu}_I$ which is related to the nuclear spin \mathbf{I} by

$$\boldsymbol{\mu}_I = g_I\mu_N\mathbf{I} \tag{16}$$

with g-factor g_I and nuclear magneton μ_N related to the Bohr magneton μ_B by the proton-electron mass ratio $\mu_N = \mu_B \cdot m_e/m_p$. The nuclear magnetic moment $\boldsymbol{\mu}_I$ interacts with the magnetic field \mathbf{B}_e originated from the total orbital angular momentum of the electron \mathbf{J} via the Hamiltonian [10]

$$\begin{aligned} H_{HFS} &= -\boldsymbol{\mu}_I \cdot \mathbf{B}_e \\ &\propto \mathbf{I} \cdot \mathbf{J}. \end{aligned} \tag{17}$$

This gives rise to further splitting of the energy levels called *hyperfine structure*. By similar reasoning as in 2.2.3 we may define the total angular momentum of the atom $\mathbf{F} = \mathbf{I} + \mathbf{J}$. Cesium-133 has nuclear spin [1] $I = 7/2$ so the two states $^2S_{1/2}$ and $^2P_{1/2}$, both having $J = 1/2$ split into hyperfine sublevels with

$$|\mathbf{F}| = F = I \pm J = \frac{7}{2} \pm \frac{1}{2} = \{3, 4\} \quad (18)$$

while the $^2P_{3/2}$ -state splits into

$$|\mathbf{F}| = F = \{I - J, I - J + 1, \dots, I + J - 1, I + J\} = \{2, 3, 4, 5\}. \quad (19)$$

For each of these sublevels the projection m_F of F onto the quantization axis can have values in the range $m_F \in \{-F, -F + 1, \dots, F - 1, F\}$ and thus, to summarize the splitting of levels described in sections 2.2.2 through 2.2.4, an illustration is seen in fig.4

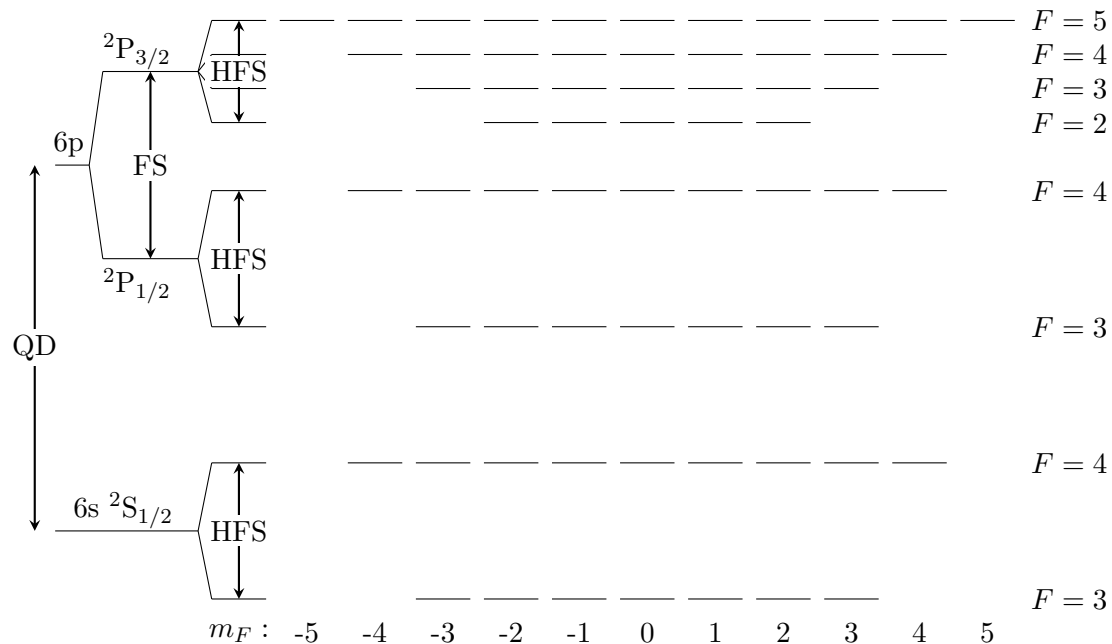


Figure 4: An illustration of sublevels for the ground state $6s$ and the first excited state $6p$ of cesium-133 including effects of quantum defect QD , spin-orbit interaction (fine structure splitting) FS and hyperfine splitting HFS .

2.2.5 Zeeman Splitting

As seen in fig.4 the energies of the m_F -sublevels of the $6s$ ground state with $F = 4$ (and $F = 3$ as well) are degenerate but by applying an external static magnetic field \mathbf{B} this degeneracy is lifted by the *Zeeman effect*. This is caused by the magnetic field interacting with the magnetic moment μ_A of the atom via the Hamiltonian [10]

$$H_Z = -\boldsymbol{\mu}_A \cdot \mathbf{B} \quad (20)$$

The total magnetic moment of the atom is comprised of both the nuclear and the electronic contributions

$$\boldsymbol{\mu}_A = g_I \mu_N \mathbf{I} - g_J \mu_B \mathbf{J} \quad (21)$$

and including also the hyperfine splitting between levels with $F = 3$ and $F = 4$ the perturbation takes the form

$$H = A \mathbf{I} \cdot \mathbf{J} - g_I \mu_N \mathbf{I} \cdot \mathbf{B} + g_J \mu_B \mathbf{J} \cdot \mathbf{B} \quad (22)$$

According to the energy splitting due to hyperfine interaction. Applying the Hamiltonian in eq.22 to the Schrödinger equation, the solution for the energy levels is given by the *Breit-Rabi* formula [27]

$$E = -\frac{h\Delta\nu}{2(2I+1)} - g_I \mu_B B m_F \pm \frac{1}{2} h\Delta\nu \cdot \sqrt{1 + \frac{4m_F}{2I+1} x + x^2} \quad (23)$$

where

$$x = \frac{(g_J + g_I) \mu_B B}{h\Delta\nu} \quad (24)$$

and $h\Delta\nu$ is the splitting at $|\mathbf{B}| = B = 0$. Notice here that x is proportional to B . For small magnetic fields we might ignore the second order term and apply a binomial expansion to the remainder of the square root and are thus left with an energy splitting which is linearly dependent on B - this is the 1st order Zeeman splitting illustrated in fig.5 for the ground state.

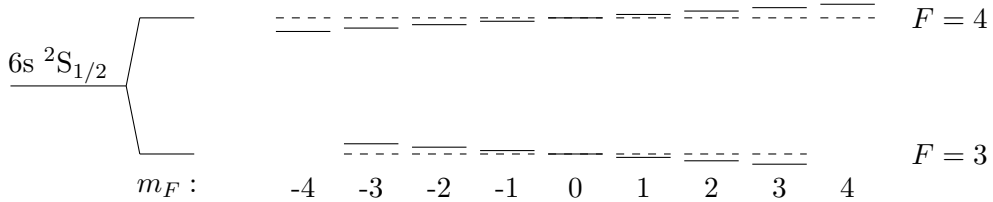


Figure 5: First order Zeeman splitting for the ground state.

Similarly we see from eq.23 that for high magnetic fields the second order term dominates the square root and in this case the dependence on B is again linear. Between the two extremes we enter an intermediate non-linear regime with second order Zeeman splitting visualized for the ground state sublevels in fig.6.

Let us dwell for a moment on this intermediate regime. Performing the MORS measurements explained in sec.2.5 we often require the strength of the applied magnetic field to be of a certain minimum - that is, we require the non-linear second order Zeeman

splitting. The important characteristic that we exploit is actually not in itself that the Zeeman splitting is of second order, but that the degree in which higher order terms deviate from linear is dependent on the m_F -quantum number. To further clarify this, we can have a look at fig.5. We can view the energy levels for say $F = 4$ as a staircase. The meaning of the quadratic Zeeman splitting, i.e. the non-linear part of eq.23, is that each step of the staircase has a unique height - the step sizes vary. The application of this will be further discussed in sec.2.5.

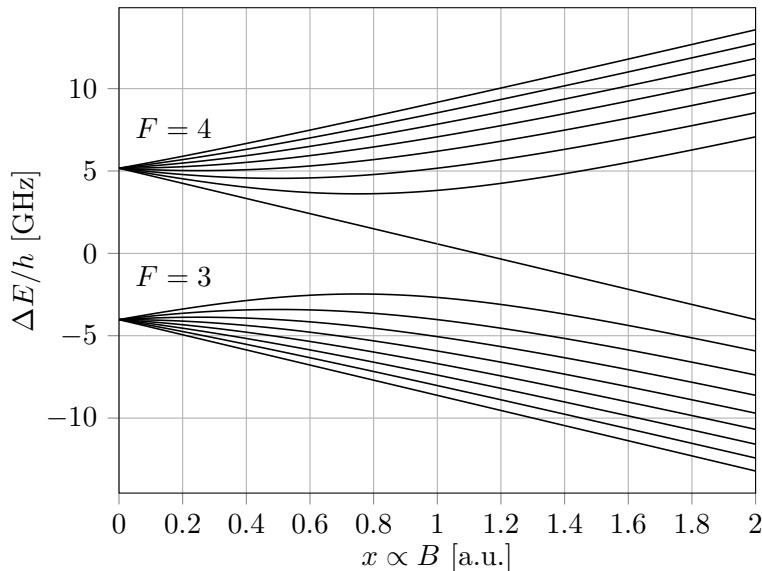


Figure 6: Zeeman splitting for all ground state hyperfine sublevels as a function of magnetic field strength (see eq.23).

2.3 Atomic Spin Ensembles

Up until now our mathematical formulation has been describing only a single atom. In reality, when performing experimental measurements, we are working not just with single atoms but with entire ensembles of $N_A \sim 10^{12}$ number of atoms. For this reason it is suitable to pose a more general description of our atomic system. The total angular momentum \mathbf{F} of a single atom described in sec.2.2.4 may be generalized to represent the total angular momentum \mathbf{J} of a collection of atoms in the form

$$\mathbf{J} = \sum_{i=1}^{N_A} \mathbf{F}^{(i)} \quad (25)$$

where i denotes the i th atom. Bear in mind here that we choose the letter \mathbf{J} not to be unreasonably confusing but to follow the notation commonly used in the literature for angular momentum. As will be clear in sec.2.5.3 it is beneficial to further specify the above equation as

$$\hat{J}_x = \sum_{i=1}^{N_A} \hat{F}_x^{(i)} \quad , \quad \hat{J}_y = \sum_{i=1}^{N_A} \hat{F}_y^{(i)} \quad , \quad \hat{J}_z = \sum_{i=1}^{N_A} \hat{F}_z^{(i)} \quad (26)$$

where we have now explicitly specified that these are quantum mechanical operators. When having a large number of atoms ($N_A \gg 1$), the component of eq.26 that points along the axis of quantization (in our case the y -axis) has approximately a continuous spectrum and may thus be substituted with its classical correspondent

$$\hat{J}_y \rightarrow J_y \quad (27)$$

while the transverse spin components \hat{J}_x and \hat{J}_z preserve their quantum mechanical features including quantum fluctuations which are dictated by commutation relations and the Heisenberg uncertainty principle

$$\left[\hat{J}_z, \hat{J}_x \right] = i\hbar J_y \quad , \quad \text{Var}(\hat{J}_x) \cdot \text{Var}(\hat{J}_z) \geq \frac{J_y^2}{4}. \quad (28)$$

This will be utilized in sec.2.5.3.

2.4 Optical Pumping

In the previous sections we explained the different atomic states and sublevels, and their origins. When working with atoms experimentally, it is often preferable to prepare atoms in specific quantum states. In this section we will explore the underlying mechanics behind the procedure of preparing such states.

2.4.1 Selection Rules

The interaction between an atom and an oscillating electric field, as in light, induces *electric dipole transitions* between two states given that the frequency of the light is close to the resonance frequency corresponding to the energy differences between two such states. Not any arbitrary transition is allowed however. When calculating the rates of stimulated transitions one would use time-dependent perturbation theory which yields certain selection rules [10]:

$$\begin{aligned} \Delta S &= 0 \\ \Delta L &= \pm 1 \\ \Delta J &= 0, \pm 1 \end{aligned} \quad (29)$$

where S , L and J are the quantum numbers described in sec.2.2.3. Just like an atom interacting with an *electric* field induces *electric* dipole transitions an applied *magnetic* field induces *magnetic* dipole transitions. In such transitions $\Delta S = \Delta L = 0$ and the corresponding selection rules are

$$\begin{aligned}\Delta F &= 0, \pm 1 \\ \Delta m_F &= 0, \pm 1.\end{aligned}\tag{30}$$

Since magnetic dipole transitions occur between states with relatively similar levels of energy compared to electric dipole transitions, such applied magnetic fields usually have much lower frequencies than electric fields - e.g. radio frequencies compared to optical frequencies.

2.4.2 Optical Pumping Scheme

Provided the knowledge of different atomic quantum states, together with the above mentioned selection rules determining which transitions are allowed, we will now turn our attention to the pumping scheme - the procedure of using light to prepare atoms in specific atomic quantum states.

Light induces different atomic transitions depending on its polarization. The quantization axis is defined by the orientation of the applied static magnetic field \mathbf{B} causing Zeeman splitting as discussed in 2.2.5. The connections between the polarization of light and the corresponding transitions are

$$\begin{aligned}\sigma^+ &\rightarrow \Delta m_F = +1 \\ \sigma^- &\rightarrow \Delta m_F = -1 \\ \pi &\rightarrow \Delta m_F = 0\end{aligned}\tag{31}$$

where $\sigma^{+(-)}$ is right (left)-handed circularly polarized light and π linearly polarized light all propagating along the axis of quantization. Experimentally we use laser light to induce such transitions. Specifically we use a *pump* laser for transitions between 6s ground states with $F = 4$ and 6p $^2P_{1/2}$ states with $F = 4$. Additionally we may use a *repump* laser for transitions between 6s ground states with $F = 3$ and 6p $^2P_{3/2}$ states. Here we include the 3 states with $F \in \{2, 3, 4\}$ due to the fact that the energy splittings between these hyperfine sublevels are small enough that the corresponding differences in frequencies lies within the Doppler broadening of the atoms, and $F = 5$ is omitted to obey the selection rules stated in eq.30. Revisiting the energy splitting between different quantum states presented in sec.2.2, including now the pump and repump lasers, an illustration is seen in fig.7. For a detailed description of the frequencies corresponding to all these different energy splittings the reader may see [2] but here it suffices to note that the pump laser is tuned to the so called D_1 -line with wavelength $\lambda \approx 895$ nm while the repump is tuned to the D_2 -line with $\lambda \approx 852$ nm. The lasers excite the atoms to states from where they naturally will decay, and in doing so the same selection rules apply. This results in the atomic states gradually over time 'moving' on average to the right in fig.7 eventually ending up in the so called *dark state* - the ground state with $m_F = 4$.

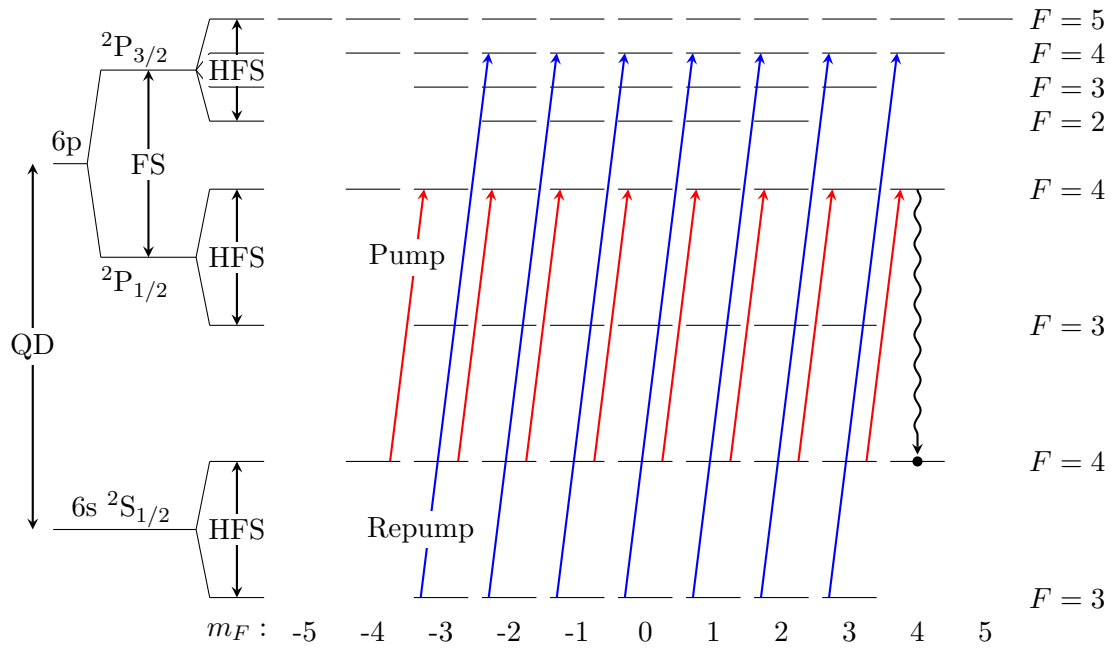


Figure 7: Energy splittings of cesium as presented in fig.4 including now the pump beam with wavelength $\lambda \approx 895$ nm and the repump beam with $\lambda \approx 852$ nm, both being σ^+ polarized.

2.5 MORS

In sec.2.4 we saw how to prepare atoms in specific quantum states by applying an external static magnetic field together with pumping laser beams. The theoretical basis of such a procedure is thus laid but in reality, to determine its degree of success, one would conduct an experiment. The method used for measurements described in this thesis is *Magneto Optical Resonance Spectroscopy* or MORS and to appreciate the mechanisms of this approach we need but to touch upon a few physical effects.

2.5.1 Larmor Precession

Assuming that our optical pumping scheme described in sec.2.4.2 has worked, we may describe our atomic state quantum mechanically as $|\Psi\rangle = |4\rangle$ meaning $m_F = 4$ - the dark state in fig.7. Let the quantization axis be along y and define the two ladder operators [12]

$$F_{\pm} = F_z \pm iF_x \quad (32)$$

such that

$$F_{\pm} |m_F\rangle = \sqrt{F(F+1) - m_F(m_F \mp 1)} |m_F \pm 1\rangle. \quad (33)$$

A measurement of the projection orthogonal to the quantization axis, say along the x -axis, would have expectation value

$$\langle F_x \rangle = \langle 4 | F_x | 4 \rangle = \langle 4 | \frac{F_+ - F_-}{2i} | 4 \rangle = 0 \quad (34)$$

due to orthogonality of different $|m_F\rangle$ states. The same result would yield itself whichever (pure) $|m_F\rangle$ state we might have, but if we were somehow able to prepare the atom in a coherent superposition like

$$|\Psi\rangle = c_3 |3\rangle + c_4 |4\rangle e^{-i\omega_L t} \quad (35)$$

where $\omega_L = (E_4 - E_3)/\hbar$, the expectation value becomes

$$\begin{aligned} \langle F_x \rangle &= (c_3^* \langle 3 | + c_4^* e^{i\omega_L t} \langle 4 |) F_x (c_3 |3\rangle + c_4 |4\rangle e^{-i\omega_L t}) \\ &= (c_3^* \langle 3 | + c_4^* e^{i\omega_L t} \langle 4 |) \frac{F_+ - F_-}{2i} (c_3 |3\rangle + c_4 |4\rangle e^{-i\omega_L t}) \\ &= \frac{1}{2i} (c_3 c_4^* e^{i\omega_L t} \langle 4 | F_+ | 3 \rangle - c_3^* c_4 e^{-i\omega_L t} \langle 3 | F_- | 4 \rangle) \\ &= \frac{1}{2i} (c_3 c_4^* e^{i\omega_L t} \langle 4 | \sqrt{8} | 4 \rangle - c_3^* c_4 e^{-i\omega_L t} \langle 3 | \sqrt{8} | 3 \rangle) \\ &= \frac{\sqrt{8}}{2i} (2i \cdot \text{Im} [c_3 c_4^* e^{i\omega_L t}]) \\ &= \sqrt{8} |c_3 c_4^*| \sin(\omega_L t + \phi) \end{aligned} \quad (36)$$

with ϕ being the phase of the complex number $c_3 c_4^*$. We would get the same result for $\langle F_z \rangle$ (except for a phase) which tells us that the spin is precessing around the axis of quantization with the Larmor frequency $\omega_L = (E_4 - E_3)/\hbar$.

2.5.2 Magnetic Dipole Transitions

In the previous section we saw how the expectation value $\langle F_x \rangle$ of the atomic spin orthogonal to the axis of quantization (y) oscillates given that the quantum state of the atom is a coherent superposition as in eq.35. The method used to prepare the atom in such a state is by *magnetic dipole transitions* which we will now investigate.

For the sake of simplicity we will restrict our attention to a two level system, say the two Zeeman sublevels of the cesium ground state with $F = 4$ and $m_F \in [3, 4]$. We wish to solve the Schrödinger equation

$$i\hbar|\dot{\Psi}\rangle = H|\Psi\rangle \quad , \quad H = H_0 + H_I(t) \quad (37)$$

using the state

$$|\Psi\rangle = c_3(t)|3\rangle e^{-iE_3 t/\hbar} + c_4(t)|4\rangle e^{-iE_4 t/\hbar} \quad (38)$$

where $|3\rangle$ and $|4\rangle$ are eigenstates of H_0 with corresponding eigenvalues E_3 and E_4 . We then apply a magnetic field \mathbf{B}_{RF} oscillating (at radio frequencies) along z so that

$$\mathbf{B}_{RF}(t) = B_{RF} \sin(\Omega t) \hat{\mathbf{z}}. \quad (39)$$

The interaction Hamiltonian is thus related to the magnetic moment $\boldsymbol{\mu}_A$ of the atom by

$$\begin{aligned} H_I(t) &= -\boldsymbol{\mu}_A \cdot \mathbf{B}_{RF}(t) \\ &= g_F \mu_B B_{RF} \sin(\Omega t) F_z. \end{aligned} \quad (40)$$

Applying first order time dependent perturbation theory the solution(s) to the Schrödinger equation becomes [12]

$$\begin{aligned} \dot{c}_3(t) &= -\frac{i}{\hbar} \langle 3 | H_I | 4 \rangle e^{-i\omega_L t} c_4(t) \\ \dot{c}_4(t) &= -\frac{i}{\hbar} \langle 4 | H_I | 3 \rangle e^{i\omega_L t} c_3(t) \end{aligned} \quad (41)$$

where again $\omega_L = (E_4 - E_3)/\hbar$ is the Larmor frequency. Combining now eqs.32 and 33 and applying to eq.40 we may write

$$\begin{aligned}
\langle 3 | H_I | 4 \rangle &= \frac{1}{2} g_F \mu_B B_{RF} \sin(\Omega t) \langle 3 | (F_+ + F_-) | 4 \rangle \\
&= \frac{1}{2} g_F \mu_B B_{RF} \sin(\Omega t) \sqrt{8} \\
&= \frac{1}{2} g_F \mu_B B_{RF} \left(\frac{e^{i\Omega t} - e^{-i\Omega t}}{2i} \right) \sqrt{8} \\
&= \langle 4 | H_I | 3 \rangle
\end{aligned} \tag{42}$$

such that eqs.41 become

$$\begin{aligned}
\dot{c}_3(t) &= -\frac{g_F \mu_B B_{RF}}{\sqrt{2}\hbar} \left(e^{i(\Omega - \omega_L)t} - e^{-i(\Omega + \omega_L)t} \right) c_4(t) \\
\dot{c}_4(t) &= -\frac{g_F \mu_B B_{RF}}{\sqrt{2}\hbar} \left(e^{i(\Omega + \omega_L)t} - e^{-i(\Omega - \omega_L)t} \right) c_3(t).
\end{aligned} \tag{43}$$

We can then do the rotating wave approximation thus ignoring the fast oscillating terms. If we assume the atom initially to be in the $m_F = 4$ state such that $c_3(0) = 0$ and $c_4(0) = 1$ we find for small t

$$c_3(t) \approx -\frac{g_F \mu_B B_{RF}}{\sqrt{2}\hbar} t \tag{44}$$

small t meaning a Taylor expansion around $t = 0$. This shows that we are able to induce magnetic dipole transitions between adjacent Zeeman sublevels with a magnetic field oscillating orthogonal to the axis of quantization defined by the static bias magnetic field.

2.5.3 Polarization of Light

Most of the measurements presented in this thesis are utilizing the interaction between laser beams and (cesium) atoms, or more specifically we exploit the effect that atoms have on the *polarization* of light. The polarization state of a pulse of light propagating in the x -direction may be described by the Stokes operators ³

$$\begin{aligned}
\hat{S}_x &= \frac{1}{2} (\hat{n}_{\sigma^+} - \hat{n}_{\sigma^-}) \\
\hat{S}_y &= \frac{1}{2} (\hat{n}_x - \hat{n}_y) \\
\hat{S}_z &= \frac{1}{2} (\hat{n}_{+\pi/4} - \hat{n}_{-\pi/4})
\end{aligned} \tag{45}$$

where $\hat{n}_{\sigma^{+(-)}}$ represents the number of $\sigma^{+(-)}$ -polarized photons and so on. Assuming now the vast majority of photons to be linearly polarized along say the y -axis we may

³Obtained and then modified from [17].

follow the same line of reasoning as in sec.2.3 when describing atomic spin ensembles. For a large number of photons $N_{\text{ph}} \gg 1$ we may substitute the Stokes operator \hat{S}_y with its classical correspondent S_y while the operators \hat{S}_x and \hat{S}_z maintain their quantum mechanical features. Following eqs.45 a photon polarized along the y -axis may be described by $\pm\pi/4$ (or σ^\pm for that matter) with equal probabilities and this results in \hat{S}_x and \hat{S}_z having a mean value of zero

$$\langle \hat{S}_x \rangle = \langle \hat{S}_z \rangle = 0. \quad (46)$$

But if we rotate the linear y -polarized light with an angle θ around the x -axis the probabilities of $\pm\pi/4$ is no longer equal. In fact, for small angles $\theta \ll 1$ we get [17]

$$\langle \hat{S}_z \rangle \approx 2\theta S_y. \quad (47)$$

This shows that \hat{S}_z contains information about the rotation of polarizations - a feature that turns out to be quite useful regarding the measuring method described in sec.2.5.5.

2.5.4 Faraday Interaction

In the previous section we presented a quantum mechanical description of the different polarization states of light. Before going into details about the actual measuring method (sec.2.5.5) we will now briefly explore a few particular effects occurring during the interaction between light and atomic spin ensembles. The absorption profile of a light beam is proportional to $1/\Delta^2$. Dispersion effects on the other hand goes like $1/\Delta$ so for a light beam sufficiently detuned from a specific transition, dispersion effects will dominate. If the atomic sample is birefringent this may influence the polarization of the light - specifically circular birefringence turn out to be very useful for our measurements. Say now that the atomic ensemble has a spin pointing along the y -axis and that a light beam linearly polarized along y is propagating in the x -direction. The spin component \hat{J}_x (described in sec.2.3) will then cause circular birefringence and thus rotate the polarization of the light. Formally one may write [17]

$$\hat{S}_z^{\text{out}}(t) = \hat{S}_z^{\text{in}}(t) + \alpha S_y \hat{J}_x(t). \quad (48)$$

The classical S_y is thus rotated around the x -axis with an angle $\alpha \hat{J}_x$ where α is describing the interaction strength. This is called *Faraday rotation* and it is a vital ingredient in the measuring scheme described below.

2.5.5 Traditional MORS

We are now ready to turn our attention to the magneto optical resonance spectroscopy method (MORS) by which several of the measurements presented in this thesis are done. A sketch of the setup is seen in fig.8.

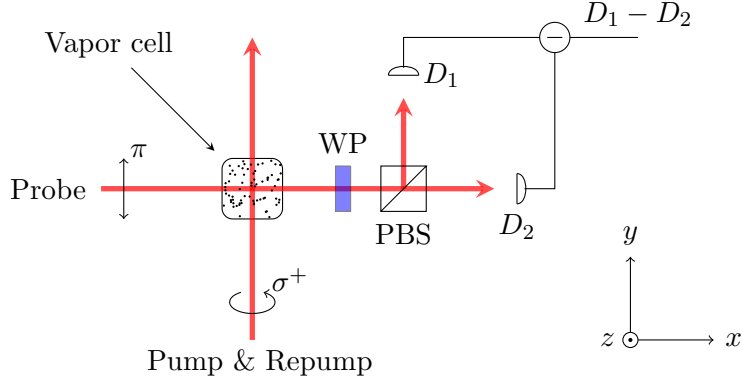


Figure 8: An illustration of the setup for conducting traditional MORS measurement. The pump and repump lasers prepare the atoms in specific quantum states and the probe laser is used to 'read' the atoms. A wave plate (WP) is used for calibration and a polarizing beam splitter (PBS) then splits the probe beam into its components, finally arriving at photo detectors D_1 and D_2 .

Our vapor cell containing cesium atoms is subjected to an external static magnetic field along the y -axis thus causing Zeeman splitting. The two σ^+ polarized pumping laser beams are used to prepare the atoms in specific quantum states and an oscillating magnetic field is applied along the z -axis inducing magnetic dipole transitions as described in sec.2.5.2. After passing through the vapor cell the π -polarized⁴ probe beam contains information about the atomic quantum states and a polarizing beam splitter splits the beam into its two components of which the intensities are finally measured by two detectors. The output is the difference in intensities between the two polarizations and the signal is sent to a lock-in amplifier which decomposes the signal into sine and cosine components. The output from the lock-in amplifier is set to give the sum of the squared amplitudes of these components and as derived in [17] this signal may be mathematically formulated as

$$\text{MORS}(\omega) \propto \left| N \sum_{m=-F}^{F-1} \frac{F(F+1) - m(m+1)}{i(\omega_{m+1,m} - \omega) - \Gamma_{m+1,m}/2} \langle \hat{\sigma}_{m+1,m+1} - \hat{\sigma}_{m,m} \rangle \right|^2 \quad (49)$$

where N is the number of atoms, $\omega_{m+1,m}$ is the frequency corresponding to the energy splitting between 'neighboring' Zeeman sublevels, $\Gamma_{m+1,m}$ is the corresponding linewidth due to decoherence and $\hat{\sigma}_{m,n}$ is the density operators describing the spin state of our atomic ensemble. A few comments on the derivation of eq.49 are worth mentioning here. We have assumed that the angle between the spin and the axis of quantization is small i.e. far less than unity. This makes physical sense if the strength of the RF magnetic field is much smaller than the bias magnetic field and thus one can ignore quadratic orders of \mathbf{B}_{RF} . Furthermore we neglect coherence terms like $\hat{\sigma}_{m,n}$ if $|m-n| \geq 2$. The

⁴In the spirit of pedantry, for this purpose any linearly polarized beam would suffice.

physical reasoning behind this makes use of the fact that resonance frequencies between Zeeman sublevels depends on m_F as mentioned in sec.2.2.5. The RF-frequency thus induces magnetic dipole transitions between only two Zeeman sublevels at a time. This means that we have an effective two-level system with the usual response with Lorentzian lineshape resulting in eq.49 being a sum of Lorentzians. Finally we assume steady state behavior of the populations $\hat{\sigma}_{m,m}$ which is reasonable e.g. when applying pumping lasers. Note here that the expectation value in eq.49 tells us that, for our MORS measurement to work, we are relying on population *differences* between Zeeman sublevels.

2.5.6 Colinear MORS

In the previous sections we explored the theory behind, and the experimental method of, conducting a *traditional* MORS measurement as they are usually performed at QUANTOP. For reasons that will later become clear this might not always be possible, or at least as straightforward, to do. As mentioned above the MORS measurement depends on population *differences* between Zeeman sublevels. This is achieved by applying our pumping laser beams as described in sec.2.4.2. But say now that we omit these two lasers. If the atoms would then be equally distributed among Zeeman sublevels we would get no signal. So one might ask how to get a signal then. The way we cope with this is by locking the probe laser to the repump transition thus essentially using a π -polarized repump beam as our probe. Since it is π -polarized it can induce only transitions with $\Delta m_F = 0$ following the selection rules of sec.2.4.1. When the atom then decays it may randomly undergo transitions with $\Delta m_F \in \{-1, 0, 1\}$ while emitting a photon with the corresponding polarization. If these three transitions had equal spontaneous rates of emission we would in the end have atoms equally distributed among Zeeman sublevels in the $F = 4$ ground state and thus no MORS signal. Fortunately though, these rates are dependent on the *Clebsch-Gordan coefficients* which vary for different transitions⁵. This results in population differences thus making it possible for us to have a MORS signal without the traditional use of pump and repump beams.

2.5.7 Vapor Cells

The dimensions of the vapor cell presented in sec.2.2 was a 5 mm cubic cell. For different reason one might wish to increase the size of the cell. The 8 different peaks in our MORS signal corresponding to transitions between the 9 Zeeman sublevels are broadened partly by decoherence processes due to atoms colliding with the inner walls of the cell. The lifetime of atomic quantum states are increased by coating the inner walls of the glass cell with an anti-relaxation surface coating in the form of a layer of paraffin [24], but this only takes one so far.

Increasing the size of the cell decreases the rate of such collisions and thus results in longer life time for an atom and hence give a more narrow peak. Furthermore, as seen in eq.49, the amplitude of the signal is dependent on the number of atoms. Increasing the dimensions of the cell along the axis of propagation of the probe beam would increase

⁵See [2] for a detailed description of these.

the optical depth i.e. the number of atoms with which our probe beam interacts, and thus give a stronger signal given the same probe power. The probe beam causes both broadening and displacement of the peaks proportional to the intensity of the probe beam. Thus with more atoms to interact with, the minimum probe beam intensity required to get a clear signal will decrease, resulting in less broadening and displacement of the peaks. So all in all it seems that the bigger the cell the better and from one point of view this is certainly true. There are however certain challenges connected with the increase of cell dimensions, one of which we will now discuss.

2.5.8 Magnetic Environment

The Larmor frequency in eq.36 is determined by the strength of the bias magnetic field and as mentioned in sec.2.5.7 our MORS signal is proportional to the number of atoms - that is the number of atoms in the same quantum mechanical state. It is clear then that subjecting all the atoms in the vapor cell to the same magnetic field strength/orientation would be preferable. For that reason we place the cell inside a cylindrical shield, like the one seen in fig.9, with several layers of different mu-metal to remove as much as possible of a random magnetic background field in our laboratory. We would then like to subject the atoms to a highly controlled, uniform and homogeneous magnetic field. This is where we encounter the first trade-off from enhancing the dimensions of the cell. For a 5 mm cubic cell we can produce a homogeneous magnetic field with e.g. a Helmholtz configuration or even better a Lee-Whiting configuration [19] but as the cell dimensions increase we need alternative methods for producing satisfyingly homogeneous magnetic fields. Inspired by [29], we set a limit on the inhomogeneity of the produced magnetic field to 3‰ as a benchmark for which to aim.

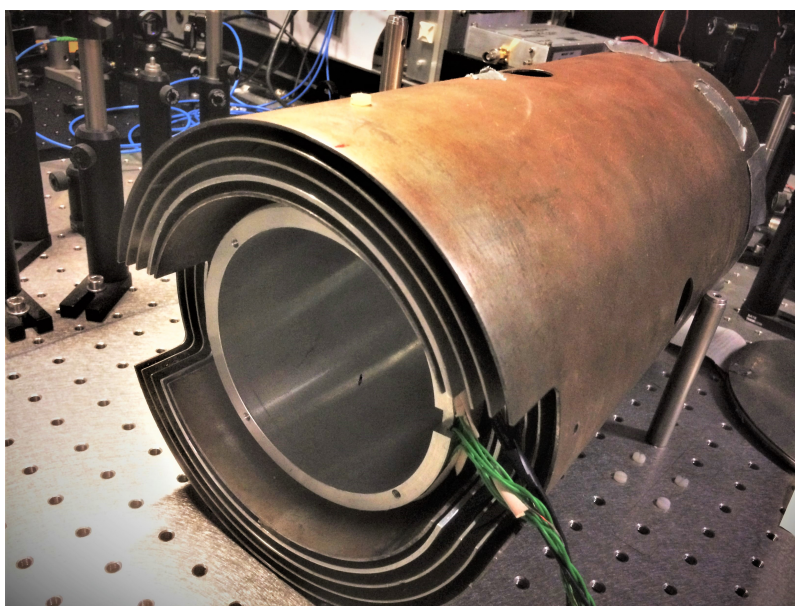


Figure 9: The 'test-shield' in which initial coil-characterizing measurements were done has several layers of different kinds of mu-metal to shield the vapor cell from the environment.

3 Magnetic Field Generation

The method we use to produce the desired magnetic fields is via printed circuit boards, or PCBs⁶. They are usually equipped with several different electronic components but we restrict ourselves simply to traces of copper through which we can send a current and exploit that electric currents produce magnetic fields. Using PCBs has several advantages including the possibility to create rather complicated traces - much more complicated than say mere circular coils in e.g. a Helmholtz configuration. Additionally PCBs are mainly composed of substrates like fiberglass which is vital to our application in that it renders them non-magnetic. We can thus create rather unique PCBs which can be mounted inside the magnetic shield without worrying about magnetic induction of the PCBs themselves and hence subject our vapor cell to a highly controlled magnetic environment.

In this section we explain the design of a PCB coil system. We introduce the mathematics behind the script used to calculate the traces on the coils and describe the essentials of the programmatic implementation.

3.1 PCB Design

A natural first step in designing the PCB coils is to determine their physical dimensions. During this process several things need to be taken into account. As mentioned in sec.2.5.8 we want to mount the vapor cell together with the PCBs inside a magnetic shield like the one seen in fig.9. The innermost shield is made of aluminum to shield from high frequency magnetic fields. It has a diameter of 11 cm and a length of 30 cm and the whole PCB configuration must fit inside this shield. To optimize the homogeneity of the produced magnetic field we want to make the PCBs as big as possible within the limitations given by this inner shield - that is, we want to maximize the distance from the coils to the cell. Furthermore we need to take into account the requirement that currents must be applied to all coils. On top of that one would, for obvious practical reasons, wish to make it as tough and durable as possible. The idea employed is to design the coils in such a way that we can put them together and the coils then sit nice and stable in the desired configuration. We also need to be able to place the vapor cell inside the coil system after assembling the system. Finally we have to make room for the pump, repump and probe lasers, mentioned in sec.2.4.2, to propagate freely.

With all these considerations taken into account we have a guideline on how to design the coil system within the given restrictions. For visual representation of the following explanations the reader may see figs.10 through 12.

In order not to put the cart before the horse, let us first define our coordinate system. Looking at fig.9 we want the probe laser to propagate along the axis of symmetry of the shield. Let us define this axis as the x -axis. Perpendicular to this, and also horizontally, we will define as the y -axis thus letting the z -axis be vertical. We begin with the design of coils that will produce magnetic fields along the z -axis and name these z -coils. While

⁶Using PCBs to create magnetic fields has previously been done in e.g. [23].

primarily intended for cancellation of the z component of any residual magnetic field, these coils can additionally be used to produce the RF-frequency field responsible for inducing magnetic dipole transitions as described in sec.2.5.2. The current that will be applied to these coils will be much smaller than for those producing the bias field. Therefore the homogeneity of the magnetic field produced by the z -coils is less critical than that produced by the bias coils. For this reason we choose the z -coils to allow for us not only to insert the vapor cell posterior to assembly but also to make room for the stem of the cell. We do this by making a hole in the center. We want to make this hole as small as possible to increase the magnetic field homogeneity, yet still large enough to accommodate the placement of vapor cells. As explained in sec.2.5.7 the goal is to use cells much bigger than the 5 mm cubic cell seen in fig.3. We inspected different versions of these longer cells that we have in the QUANTOP laboratories, to determine the size of the hole in the z -coils. As seen in fig.31 these cells have an inner square cross section tube containing the cesium vapor. This is enclosed by an outer cylindrical tube from which a stem, containing a droplet of solid cesium, extends. When applying the pump/repump lasers we would prefer the propagation of these to be perpendicular to the sides of the inner rectangular shaped glass tube in order to minimize diffraction. This causes limitations of the rotational orientation of the cell. More specifically this sets restrictions to the orientation of the stem which in effect defines the minimum size of the hole in the z -coils. For several different (long) cells we measure the distance from the end of the cell to the stem together with the angle between the stem and a given side of the inner rectangular shaped glass tube. This defines the size of the hole. Next, we want to design the coil system in such a way that we can assemble it in a manner similar to children's toys so that it remains in the desired configuration without being too fragile. For that reason we make small holes in the z -coils for the other coils to 'click' into.

Furthermore we wish to let the z -coils carry current to the other two pairs of coils. We do this by making room in the corner of the PCB for a collective pad to which we can connect wires carrying the in and outgoing currents. From this pad, we put traces along the outskirts of the z -coils to a place where the two PCBs conveniently meet.

Finally we need to decide the overall dimensions of the PCBs. We choose a length of 24 cm giving us 3 cm of free space at each end of the shield, for wires etc. An illustration of this preliminary design of the z -coils is seen in fig.10.

We now turn to the design of the y -coils. These will be used to produce the static bias magnetic field constituting the axis of quantization and may thus be the most important ones in terms of homogeneity. With most of the restrictions considered in the design of the z -coils there are but a few things we need here. For assembling we let the y -coils have two hooks at each end to 'grab onto' the z -coils. One pair of such hooks will be responsible for carrying the current from one z -coil to the other, running along the edge of the y -coil. Of the other pair of hooks, one will be connected to the z -coil in order for current to flow. Finally we need to make room for the pump/repump beam to traverse the y -coils. For this reason we make an elongated slit so as to make it possible for the

pumping beams to hit the entire vapor cell. An illustration of the y -coils is seen in fig.11.

Lastly, for the x -coils we barely need any further considerations. For assembling we make extensions on each side so as to fit into the slits of both y and z -coils. On one side we make room for in and outgoing current from and to the z -coils. Finally we make a hole in the center to allow the probe beam to propagate freely (see. fig.12).

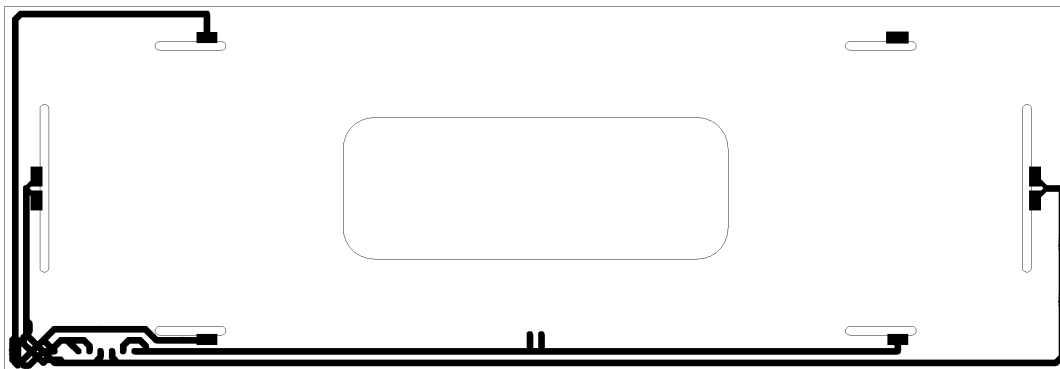


Figure 10: Preliminary design of Z-coils. In the bottom left is a HUB from which the other PCBs are supplied with currents. Thin lines mark the edges of the PCB while thick lines represent traces of copper.

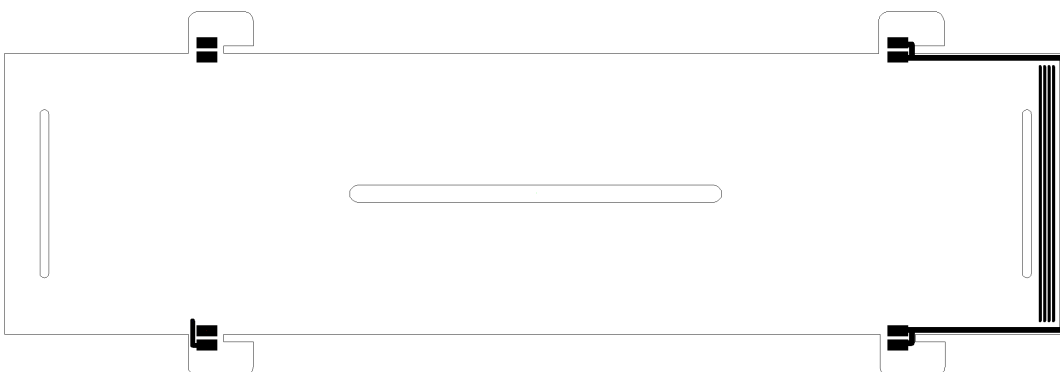


Figure 11: Preliminary design of Y-coils. In the bottom left is the in and output for current. On the far right, traces are placed to run current from one Z-coils to the other. In the center is a slit to make room for pumping lasers.

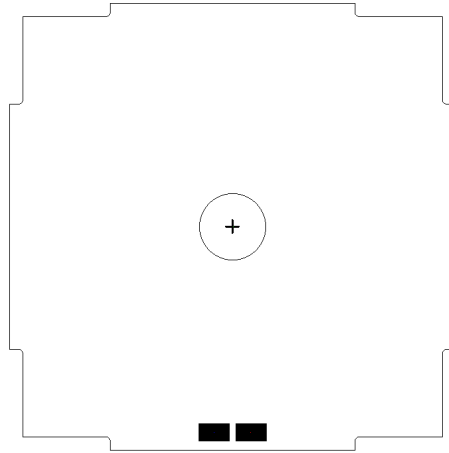


Figure 12: Preliminary design of X-coils. In the bottom we have in and output for current, and in the center we have a hole for the probe beam to propagate through.

3.2 Mathematical Basis

With the preliminary design of the different pairs of PCB coils in place, the next step is to figure out how to place the traces of copper. The natural question then is how to choose a specific set of traces and determine the optimal design of the PCBs. The traces for all PCBs used in experimental work for this thesis was calculated using a script written by Jürgen Appel during his time working as an associate professor at NBI. For the sake of the reader we will exclude most of the programmatic details and reckon it sufficient but to declare the fundamental headlines. To fully appreciate these however, we require an insight to the mathematical foundation upon which the script has been developed.

In the spirit of simplification let us focus only on one pair of coils, say the z -coils. The following can then easily be generalized to the other coils. To clarify the task at hand, an illustration of the geometry is sketched in fig.13.

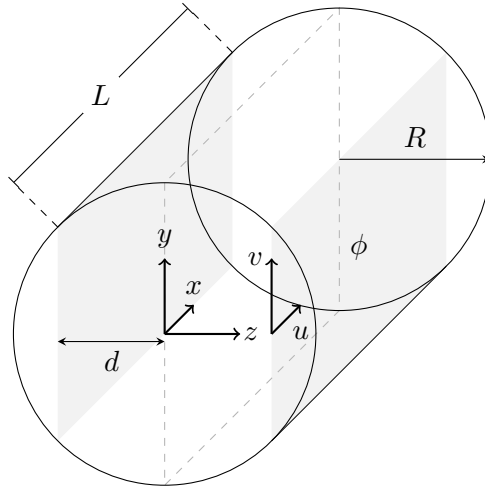


Figure 13: An illustration of current sheets (PCB coils) mounted inside a cylindrical magnetic shield.

Let us begin by defining an xyz coordinate system with the origin on the axis of symmetry of the cylinder at one end. To avoid confusion we let coordinates u and v describe points on the current sheets, or PCBs, which for now is assumed to be infinitely thin. These are represented by the gray areas in fig.13. They are located at a distance d from the xy -plane. The cell is located on the x -axis and in the case of an 8 cm long cell it will be located *along* the x -axis. The exercise to be undertaken is to find a way to calculate the traces on the current sheets so as to minimize the magnetic field inhomogeneity inside the volume of the cell. The method employed is to define a scalar field $\phi(u, v)$ on the current sheets. Since we know that currents will run in the uv -plane we define it in a way such that the curl of this scalar field times the normal vector to the plane is the current density. Mathematically formulated we have

$$\begin{aligned} \mathbf{j} &= \nabla_{uvd} \times \begin{pmatrix} 0 \\ 0 \\ \phi(u, v) \end{pmatrix} \cdot (\delta(z-d) + \delta(z+d)) \\ &= \begin{pmatrix} \partial_v \phi \\ -\partial_u \phi \\ 0 \end{pmatrix} \cdot (\delta(z-d) + \delta(z+d)) \end{aligned} \quad (50)$$

with \mathbf{j} being the current density. Note here that, for any pair of coils, we demand the two current sheets to have both identical traces *and* to be identically oriented. Strictly speaking, this might not be completely necessary but it reduces to some degree the number of calculations, and from a perspective of symmetry it arguably appears rather reasonable. Now, defining the current density as in eq.50 ensures that the current runs in the plane of the PCBs. We then need to relate this current to magnetic fields \mathbf{B} inside the vapor cell. For this we use classical electromagnetism and apply Biot-Savart's law which is given by [13]

$$\mathbf{B} = \frac{\mu_0}{4\pi} \iiint \frac{\mathbf{j} \times (\mathbf{r} - \mathbf{r}')}{|\mathbf{r} - \mathbf{r}'|^3} d^3\mathbf{r}' \quad (51)$$

where \mathbf{r} represents a point inside the cell, \mathbf{r}' a point on the current sheets with μ_0 being the vacuum permeability. Combining eqs.50 and 51 we get

$$\mathbf{B} = \frac{\mu_0}{4\pi} \sum_{z=\pm d'} \iint \frac{\begin{pmatrix} \partial_v \phi \\ -\partial_u \phi \\ 0 \end{pmatrix} \times \begin{pmatrix} x - u \\ y - v \\ z - d' \end{pmatrix}}{\left| \begin{pmatrix} x - u \\ y - v \\ z - d' \end{pmatrix} \right|^3} dudv. \quad (52)$$

By this we have related the magnetic field \mathbf{B} inside the cell to the current density \mathbf{j} on the PCBs, but in reality there would also be a contribution to the magnetic field due to induced magnetization of the shield. That is

$$\mathbf{B} = \mathbf{B}_I + \mathbf{B}_m \quad (53)$$

where I represents the current and m represents magnetization. To include the latter in the calculations would, to a higher degree, be in accordance with what magnetic field is actually present inside the cell, but this is a bit more cumbersome.

For now, we will ignore this effect and proceed with the description of the script. The interested reader may review appendix A for an explanation on the theory of how to implement the effect from shields in the calculations.

3.3 Programmatic Implementation

In this section we will explore the key points of the script that handles the calculations of the current traces on all PCBs used in experimental work of this thesis.

The initial task is to find a way to go from the scalar field $\phi(u, v)$ on the current sheets to the magnetic field $\mathbf{B}(x, y, z)$ at target points inside the cell. This is theoretically done via eq.52. As with all computational maneuvers, though, one has to discretize when incorporating calculations consisting of continua. For the current sheets illustrated in fig.13 we create a two-dimensional mesh grid of pixels to represent the PCBs. Similarly we represent the volume of the vapor cell with a three-dimensional mesh grid. The resolution used for the PCBs are one pixel per millimeter while the cell volume is represented by a $5 \times 5 \times 11$ grid. The script then assumes an infinitely thin current loop around each pixel, carrying the same current for each pixel, and calculates the magnetic field, produced by these loops, at each target point. We then define the desired magnetic field at each target point. Since we want to maximize magnetic homogeneity this could, e.g. in the case of z -coils, be

$$\mathbf{B}_{\text{target}} = \begin{pmatrix} 0 \\ 0 \\ B_z \end{pmatrix} \quad (54)$$

where $B_z = 1$ G. The magnetic field strength here is chosen arbitrarily since, as implied by eq.51, it is linearly proportional to the applied current.

We now wish to find a linear superposition of these fields, produced by the many current loops, such that the produced fields fit exactly. To clarify we may write

$$\begin{pmatrix} \mathbf{B}_{111} \\ \mathbf{B}_{112} \\ \vdots \\ \mathbf{B}_{211} \\ \vdots \\ \mathbf{B}_{311} \\ \vdots \end{pmatrix} = \mathbf{A} \cdot \begin{pmatrix} \phi_{11} \\ \phi_{12} \\ \vdots \\ \phi_{21} \\ \vdots \end{pmatrix} \quad (55)$$

where $\mathbf{B}_{ijk} = (B_{ijk,x}, B_{ijk,y}, B_{ijk,z})$ is the vector describing the target field at the mesh grid target point (i, j, k) and ϕ_{lm} is the scalar field $\phi(u, v)$ at mesh grid pixel point (l, m) . Finding the desired linear superposition is thus equivalent to finding the ϕ -vector in eq.55. Since there are many possible solutions for $\phi(u, v)$ that gives the desired field, this allows for an optimization with the boundary condition that the produced field is exactly the desired one. One example would be to find the solution that minimizes dissipation. In our case we choose another optimization - the one that minimizes self-inductance. That is, we want to minimize

$$\iint \nabla^2 \phi(u, v) du dv \quad (56)$$

using the condition that ϕ solves eq.55. The reasoning behind this choice of optimization is that it is also the one that spreads out the currents and therefore makes the traces lie as far apart from each other as possible. This is indeed a preferable solutions in that we do not want currents to flow arbitrarily free between traces.

Now that we have found ϕ our approximations begin. As mentioned we have an infinitely thin closed loop around each current sheet pixel. We need to somehow make one line out of all these loops. By considering all pixels and superposing all current loops we get effective current loops that may circumfere many pixels. Furthermore, in some loops the current runs clockwise while in others it runs counterclockwise thus necessitating intersections. We cope with this by duplicating the same traces into two planes, with connections between them, while having the currents run the right way such that the fields of both planes ideally add identically.

If we view the scalar field ϕ as a landscape, the traces will run along the contour lines. These lines are made as broad as possible around their center in order to minimize resistance. We assume no voltage gradient transversal within each trace meaning that we

assume a homogeneous and centered current. In this case 'as broad as possible' is of course within a sensible limit, the point being that, at places where the contour lines lie closely together, we define a minimum distance between two adjacent lines which in effect limits their widths.

Another thing taken into account is the finite size of the PCBs. The traces naturally need to lie within the physical boundaries of the PCB, and the above calculations are performed within the limits of having a specified maximum number of contour lines within this area.

Finally, the produced traces are mapped onto their respective sheets via files like the ones seen in [figs.10](#) through [12](#). The last step in the production of our coil system is then to transform this into actual PCBs. For this we use a program called *Eagle*, which is a software developed by *Autodesk*, with the specific purpose of designing PCBs. The final product is then produced by the company *JLPCB* [\[6\]](#) located in HongKong. The interested reader may visit [appendix B](#) for illustrations of the final traces used to produce the coils.

4 Coil Characterization

In this section we present the process of characterizing the coils. We describe initial testing of the PCBs and after assembling the coil system we present characterization of the produced magnetic field and try to optimize the geometry. Finally we examine the process and effect of demagnetization of magnetic shields.

4.1 Assembly

After the delivery of the fabricated coils, a natural first step is to check that they work as desired. Unfortunately though, they arrive with a few errors. When trying to measure the resistance of the z -coils we conclude that no connection is found between the in and output. It turns out that one of the pins that connect the two sides of the PCBs is missing, and we are able to locate the mistake and connect the two sides ourselves. Another error regarding the z -coils is a short between the traces that supplies current to the other coil pairs. This we are able to correct simply by cutting the copper trace at the location of the unwanted connection. As for the x -coils however, we are not as lucky. Apart from the fact that the hole, through which the probe beam is intended to propagate, is missing, several of the pins connecting the two sides of the PCB have unwittingly been omitted. Now, the x -coils are meant to produce magnetic fields along the x -axis, but the magnetic shield seen in fig.9 has in fact circular coils wound around the inner aluminum shield, which produce magnetic fields with the same orientation. On top of that, the x -coils are the smallest ones, and they also have the largest distance to where the vapor cell is supposed to be mounted. With these considerations taken into account we decide to include the x -coils in the assembly simply for structural stability, but not to connect any current to them. In the case we need an x -component of magnetic field to cancel out the background field we can use the coils that are already present in the shield.

With all the above corrections in place, we are ready to put together the complete system of coils. A picture of the final product is seen in fig.14 where we have included 3D-printed holders enabling us to position the coil system symmetrically around the axis of symmetry of the shield.

4.2 Cell Measurements - Outside Shield

Now that we have assembled the coil system in its desired configuration, we naturally wish to characterize its produced magnetic field. Since it is mildly cumbersome to mount the system inside the magnetic shield, we begin by identifying the magnetic field created outside the shield.

We mount a 5 mm cubic vapor cell on a post, and place the coil system on rails in order to be able move it so as to measure the field at different positions. At each position we conduct a co-linear MORS measurement as described in sec.2.5.6. Since the y -coils are to be used for the bias magnetic field, the homogeneity of these are most critical, so we focus on those for now. We apply a current of 1.1 A to the y -coils while using the



Figure 14: Picture of the assembled coil system.

z -coils for RF-frequencies (see sec.2.5.2). The frequency ω_{RF} of the z -coils is linearly swept through a frequency range within three seconds and fig.15 shows a plot of raw data obtained from one position.

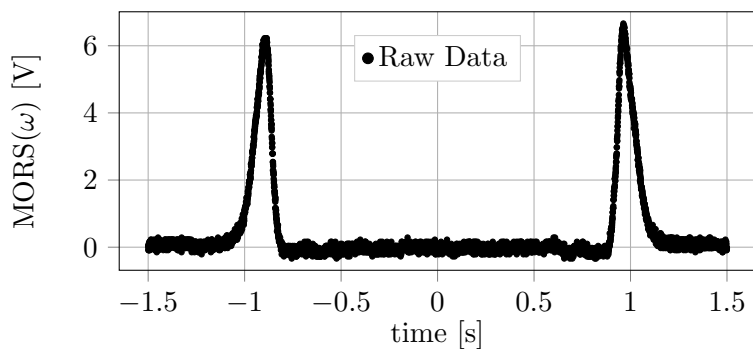


Figure 15: An example of raw data from initial coils characterization outside magnetic shield. During the interval $t \in [-1.5, 0]$ the RF-frequency undergoes an up-sweep, meaning it is linearly increasing as a function of time, while $t \in [0, 1.5]$ is a down-sweep.

The reason we see two peaks is that the first half where $t < 0$ is an up-sweep meaning increasing ω_{RF} while the second half ($t > 0$) is a down-sweep. The plot in fig.15 is essentially two MORS signals but for now let us focus on just one. The MORS signal in

eq.49 is a sum of eight Lorentzians, each one corresponding to a coherent superposition of adjacent Zeeman sublevels, so one might ask why we only see one peak. This is due to the fact that each of these eight peaks have a certain width caused by decoherence processes. When this broadening gets large enough the eight peaks overlap and combine to one. Notice, however, that fig.15 does not quite have peaks resembling Lorentzians - they seem somehow skewed. This may be due to magnetic inhomogeneities, or it may be due to the RF-frequency being swept too fast.

During this initial coil characterization we are interested in measuring the magnetic field - that is, we want to measure the Larmor frequency. So to fit the full MORS eq.49 to the data in fig.15 seems to over complicate the task at hand. There would be too many fitting parameters which are not essential to the purpose of this particular measurement, so to estimate the Larmor frequency we simply select the 20% of data points with the highest amplitude and take the mean time (x -axis) and convert this mean into the corresponding frequency. For each data set we get two estimates of the Larmor frequency - one for the up-sweep and one for the down-sweep. The mean of those two then constitute our estimate

$$\omega_{L,est} = \frac{\omega_{L,upsweep} + \omega_{L,downsweep}}{2}. \quad (57)$$

In reality the Larmor frequency is determined by the strength of the total magnetic field, including all directions. That is

$$\omega_L \propto |\mathbf{B}| = \sqrt{B_x^2 + B_y^2 + B_z^2}. \quad (58)$$

The magnetic background field may point in an arbitrary direction, so if we assume the y -coils to only produce magnetic fields in the y -direction we can write

$$|\mathbf{B}| = \sqrt{B_{x,BG}^2 + (B_y + B_{y,BG})^2 + B_{z,BG}^2} \quad (59)$$

where BG means background and B_y is the field produced by the coils. With an applied current of 1.1 A the produced magnetic field is on the order of 1 G, so we assume $(B_y + B_{y,BG})^2 \gg B_{x,BG}^2 + B_{z,BG}^2$. We can thus do a binomial expansion of eq.59 to get

$$\begin{aligned} |\mathbf{B}| &= \sqrt{(B_y + B_{y,BG})^2 \left(\frac{B_{x,BG}^2}{(B_y + B_{y,BG})^2} + 1 + \frac{B_{z,BG}^2}{(B_y + B_{y,BG})^2} \right)} \\ &= (B_y + B_{y,BG}) \sqrt{1 + \frac{B_{x,BG}^2}{(B_y + B_{y,BG})^2} + \frac{B_{z,BG}^2}{(B_y + 2B_{y,BG})^2}} \\ &\approx (B_y + B_{y,BG}) \left(1 + \frac{B_{x,BG}^2 + B_{z,BG}^2}{2(B_y + B_{y,BG})^2} \right) \\ &= B_y + B_{y,BG} + \frac{B_{x,BG}^2 + B_{z,BG}^2}{2(B_y + B_{y,BG})}. \end{aligned} \quad (60)$$

From this we see that when characterizing the y -coils, the y -component of the background field has a bigger impact on the Larmor frequency than does the x or z components. When B_y and $B_{y,\text{BG}}$ point in the same direction they add up, resulting in a minor increase in the Larmor frequency. Similarly, when pointing oppositely the Larmor frequency slightly decrease. To cope with this we do two measurements for each position of the cell - the difference being that we flip the current applied to the coils, which in effect changes the direction of the produced magnetic field. We can thus estimate the Larmor frequency due to the coils by taking the mean of the two

$$\omega_L = \frac{\omega_L^+ + \omega_L^-}{2} \quad (61)$$

where \pm indicates the direction of the current such that ω_L^\pm are given by eq.57. The result of this series of measurements is seen in fig.16.

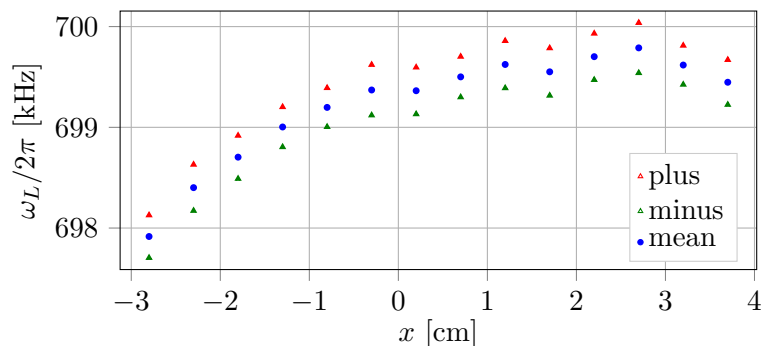


Figure 16: Measurements of Larmor frequencies obtained from initial coil characterization outside the magnetic shield.

When interpreting this result, we note several things. First of all we see that, over the total range of positions, the magnetic field varies $\sim 3\%$ which is actually a relatively acceptable start. Secondly, the data points are obviously asymmetric which, at first glance, might seem slightly worrying, but there are a few reasons for why this might be. Due to the way the cell was mounted, we were able to position the cell slightly further in one direction. This would be on the order of < 1 cm so that the position that corresponds to the cell being in the exact center of the coil system is somewhere between $x = 0$ cm and $x = 1$ cm. But even when taking this into account we still see an asymmetry. We conclude that this is probably due to the fact that, when changing the position of the cell relative to the coil system, in reality we move the coils and not the cell. There are many optical components close to the coils, all of which might cause a certain amount of magnetic induction. This may affect the resulting magnetic field at the location of the cell, and by moving the coils relative to these optical components it may cause varying effects depending on the position of the coils.

For now we cease further exploration into this preliminary coil characterization which suffices to achieve a precursory insight to the produced magnetic field. At the end, we

are interested in the magnetic profile inside the magnetic shield.

4.3 Cell Measurements - Inside Shield

Magnetic shields like the one seen in fig.9 is designed to shield the inside from external magnetic fields. But whatever way we then choose to produce magnetic fields inside the shield, these layers of mu-metal cause some amount of magnetic induction thus changing the magnetic field profile compared to outside the shield. With the measurements presented in sec.4.2 it is therefore interesting to place the same configuration of coils inside the shield and then conduct similar series of measurements. Two such series is the content of this section.

When conducting the measurements presented in the previous section we applied a current of 1.1 A to the y -coils. In doing so however, we noticed that the coils became rather hot. Inside the shield there is even less circulation of air so they will become even hotter. Since our focus of these measurements is to explore the homogeneity of the coils and not the magnetic-field-strength-to-applied-current ratio, we begin by adjusting the current to roughly half of what we had in sec.4.2.

When performing the measurements outside the shield we moved the coils relative to the cell and not vice versa. In the present case, that is not preferable due to induced magnetization caused by the shield. We therefore place the coil system in the center of the shield and move now the vapor cell between measurements. To ensure that the coils are perfectly centered inside the shield we 3D-print a holder that matches both the dimensions of the inner shield and the ends of the coil system. The results of this measurement series is seen in fig.17 where again we apply both plus and minus current at each position of the cell.

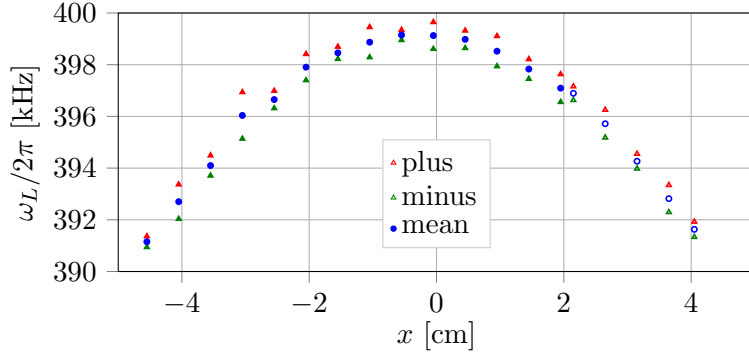


Figure 17: Measured Larmor frequencies during initial coil characterization inside the magnetic shield.

Due to the mounting of the cell we were still limited regarding the positioning of the cell. Thus, the position corresponding to the cell being exactly in the center of the shield is somewhere between $x = 0$ cm and $x = -1$ cm. We see that the magnetic field profile is

much more symmetric. This indicates that the assumption that moving the coils rather than the cell gave a misrepresentation of the profile, was probably right. Next, a rather peculiar observation was done when looking at fig.17. Notice that the red and green points correspond to plus and minus currents respectively. For each cell position these two data points are combined to give the blue point which is the field produced by the coils. This means that the difference between the blue and say the red is due to the residual magnetic field. When looking through the data it seems to indicate that the background oscillates (spatially). Our best guess for the reason as to why that might be, is that the direction of the current actually has an effect on the magnetic shield. Every other cell position in fig.17 was measured first with a plus current and then with a minus current. The other half was measured first with a minus current, then with a plus. This may actually turn out to be a somewhat useful observation, and we will return to this in sec.4.4.4 when talking about demagnetization of the magnetic shield. Another noteworthy remark regarding the plot in fig.17 is visualized by the change of marker styles around $x = 2$ cm. Given the way in which the vapor cell was mounted, we were not able to measure further. We then rotated the mount holding the cell 180° to allow for further measurements and this is indicated by the change in marker styles. The magnetic homogeneity, on the other hand, has become worse by mounting the coil system inside the shield. The variation of magnetic field, over different cell positions, has now increased to $\sim 2\%$. Since the configuration of the coil system is exactly the same as for the measurements performed outside the shield, this gives a first glance at what effect the shield might have on the magnetic field profile. If our aim of homogeneity is a variation on the order of sub-per mil, we obviously still have some optimization to do. Before turning to that, though, we conduct yet another measurement series inside the shield.

To see whether the magnetic field homogeneity is dependent on the strength of the field, we now decrease the applied current even more - a factor of about 10. The results of these measurements are seen in fig.18.

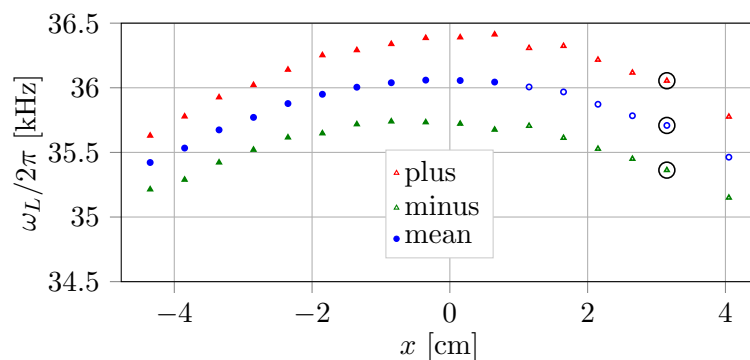


Figure 18: Magnetic field profile inside the shield - now with a lower current applied to the coils.

It is appropriate here to explain why the data at one of the positions in fig.18 has circles around them. The oscilloscope that was used to store the data froze when we reached this cell position. When analyzing these data we noticed that the data points for one of the positions was missing due to a defect file. Furthermore the three points (two measurements) with circles around them was actually given a name that suggested they belonged to the neighboring position. But given the awareness of the break in the measurements due to the equipment, together with previous measurements - especially the one presented in fig.17 - we conclude that these points most probably correspond to the position given in fig.18. This is of no particular relevance to the overall conclusion, but simply a justification of posterior manipulation of these two data points.

Regarding the homogeneity of the magnetic field we see again a variation of $\sim 2\%$ over the different cell positions which indicates that the applied current does not have a big effect on the homogeneity. However, the oscillating difference in the background field seen in fig.17 now seems to have disappeared. This may indicate that, at lower Larmor frequencies, i.e. lower magnetic fields, the 'memory' of the shield become less significant.

At this point in our endeavor we might benefit from stepping back and regaining an overview. We have designed what was thought to be an optimal system of coils, but during characterization we find that the magnetic field homogeneity does not live up to neither our hopes nor our expectations. We contemplate a lot of different ideas about how to advance. One idea is to design yet another set of coils, specifically designed to cancel out the curvature of the magnetic field profile seen e.g. in fig.18. For several reasons this turns out not to be particularly successful, though, but we will eventually return to a similar idea in sec.4.5.1. At this moment several challenges have arisen. The script described in sec.3.3 actually calculates the expected magnetic field from the resulting traces, but there is a discrepancy between this expected magnetic profile and the ones measured experimentally. Since the PCB traces are so untraditional we do not have an analytical solution to the magnetic field to which we can compare the expected profile. In fact we even try to force the script to create a Helmholtz configuration, to which an analytical solution is readily obtained, with the hope that we can compare the two. In doing so we conclude that they essentially agree - the difference being so small that we assume the main reason is the discretization of the current sheets. Need be said that the script in its entire complexity remains, even as these words are written, to a certain degree a black box to the author of this thesis.

At this point, however, we get the idea that the discrepancy between the expected and the measured magnetic profiles may be due to the fact that the script does not take into account the finite thickness of the PCBs (we later learn that this is actually not the case). This leads us to turn the bucket upside down and approach the situation not from a theoretical and computational point of view, but rather from an experimental angle. We choose to explore how the magnetic field profile changes with varying separation distances between pairs of PCBs. One reason to do this is the pursuit of further clarification of the discrepancy between predicted and measured magnetic fields. Another reason is the hope that, from this, an idea of how to approach optimization of the coil system

emerges. These measurements were however not conducted in the same manner as those presented so far.

4.4 Optimizing Coil Design

The different series of measurements presented in the following sections are not done by the MORS method as was the case in the previous sections. The magnetic fields will now be measured by a USB probe containing, among other things, a magnetometer.

4.4.1 The Probe

The device we will be using in the following measurements is a USB probe like the one shown in fig.19. It is a *BNO055* USB stick [3] containing both an accelerometer, a gyroscope and a magnetometer. We will exclusively be utilizing its magnetometric abilities. In fig.19 we see three black chips - the one to the left is the part used for measuring magnetic fields. It has three axes which enables us to measure not only the total magnetic field strength, as with the MORS method, but also to measure the orientation of the magnetic field.

To remind ourselves, the reasoning behind performing the following measurements is to get a deeper understanding about the discrepancy between the magnetic profile predicted by the script, and the profile obtained experimentally. We will here be focusing on the y -coils, and we will try to explore how the magnetic profile changes with different distances between the two coils. We begin by measuring the field in the absence of a magnetic shield.



Figure 19: A *BNO055* USB probe used to perform magnetometry.

4.4.2 Outside Shield

The y -coils were originally designed to be separated by 63.4 mm. Based on this distance, the script then calculated the optimal trace pattern. For measurements outside the shield we measure the magnetic profile for seven different distances ranging from 58 mm to 78 mm. An example of one such measurement is seen in fig.20.

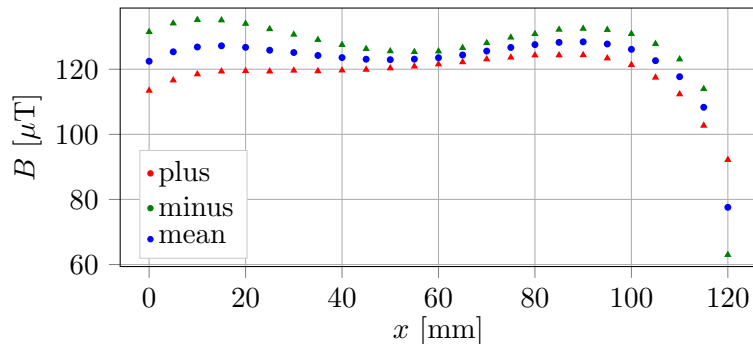


Figure 20: USB-probe measurements of magnetic field of y -coils separated by 78 mm. Relative standard deviation of data points in the range $x \in [10, 90]$ is 1.5 %.

To have a consistent and quantitative way of comparing the homogeneity of the magnetic profile for the different distances, we calculate the relative standard deviation of data points in the center 8 cm. Note that the resolution, meaning number of points per length, are the same for all seven distances. To clarify, as seen in fig.20, this corresponds to data points in the range $x \in [10, 90]$.

To compare with the magnetic profile predicted by the script, we take the traces of the produced coils, and then redefine the distance between the coils. We then calculate the expected field at points corresponding to the data in fig.20 and similarly calculate the relative standard deviation of these. The results for comparison are presented in table 1, where we clearly see a discrepancy between the predicted and the measured magnetic profiles.

Distance [mm]	58	59	63	65	70	73	78
Predicted std_{rel}	3.8 ‰	3.4 ‰	1.4 ‰	0.4 ‰	2.7 ‰	4.5 ‰	7.7 ‰
Measured std_{rel}	3.4 ‰	3.2 ‰	2.7 ‰	2.7 ‰	2.1 ‰	1.9 ‰	1.5 ‰

Table 1: A comparison of the relative standard deviation of the measured and the predicted magnetic profiles for the y -coils separated by different distances. Be aware to distinguish between ‰ and ‰.

Some of this discrepancy we may be able to account for. The points used to calculate the predicted fields all lie on the x -axis. The part of the USB probe that does the actual measuring has a volume of $1.3 \times 3.8 \times 5.2 \text{ mm}^3$ [11], and we are not confident about the location of the magnetometer inside this volume. Furthermore we may not have been able to locate this part of the USB probe exactly on the x -axis. We might thus be measuring slightly off axis, which would mean a decrease in the magnetic homogeneity, but it does not at all account for the discrepancies seen in table 1. This actually, to this day, remains a bit of a mystery, but in the end we are primarily interested in the magnetic field produced by the coil system when mounted inside the magnetic shield.

4.4.3 Inside Shield

We now wish to perform measurements similar to the ones presented in the previous section, but now inside the magnetic shield. We will again use the USB probe seen in fig.19 as our measuring device, which is not straightforward to mount inside the shield. In order to obtain the magnetic profile we need to be able to move the device, along the axis of symmetry of the shield. Our solution is to use a hollow glass tube with a diameter big enough to contain the USB probe, and yet small enough to fit through the hole in the end cap of the shield. We strip the USB stick of its original case and 3D print a holder to fit exactly inside the glass tube as visualized in fig.21a. We then mount the glass tube to a rail in order to enable movement of the probe, along the axis of symmetry (fig.21b).



(a) USB probe mounted inside the glass tube.



(b) Glass tube mounted on rails and USB probe inside the shield.

Figure 21

We choose to separate the y -coils by five different distances ranging from 51 mm to 78 mm. The magnetic profile measured for a separation of 78 mm is seen in fig.22. Note that the exact same coil configuration (i.e. separation distance) is used to produce the data shown in figs.20 and 22, the difference being the former is performed outside the shield and the latter inside. We find again a relative standard deviation of points over 8 cm to be 1.5%, but this is a rather arbitrary coincidence given that the profile has clearly changed due to the effect of the shield. In fact, contrary to the measurement series outside the shield where the magnetic field homogeneity increased with increasing separation, we see the opposite effect inside the shield. For a 78 mm separation the curvature of the profile is negative. As the coil separation decreases the curvature increases (becomes less negative). When we reach a separation of 51 mm the curvature gets very

close to zero as seen in fig.23. This is a rather satisfying result since zero curvature means perfect magnetic homogeneity. In the case of 51 mm separation the relative standard deviation of the measured magnetic field over 8 cm is 0.8 ‰. In terms of homogeneity of magnetic field strength, this is the best result we have been able to obtain.

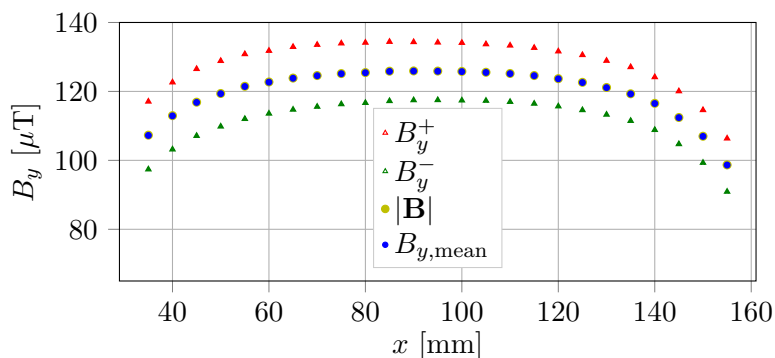


Figure 22: USB probe measurements of magnetic fields produced by the y -coils separated by 78 mm. The relative standard deviation of data points in the range $x \in [55, 135]$ is 1.5 ‰.

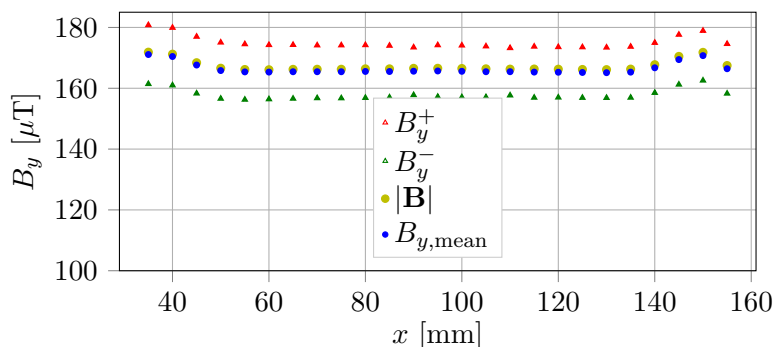


Figure 23: USB probe measurements of magnetic fields produced by the y -coils separated by 51 mm. The relative standard deviation of data points in the range $x \in [55, 135]$ is 0.8 ‰.

Distance [mm]	78	65	63	58	51
Measured std_{rel}	1.5 ‰	7 ‰	...	3 ‰	0.8 ‰

Table 2: Relative standard deviation of measured magnetic fields from seventeen data points over 8 cm. The magnetic field is produced by the y -coils separated by five different distances inside the shield.

4.4.4 Degaussing

Now that we have decided on the optimal coil configuration, we return to the MORS method, which means that we will again be using the z -coils for RF-frequencies. After reassembling the full coil system and mounting it inside the shield, our aim is now to examine to which degree the magnetic field homogeneity has improved when applied to the vapor cell.

As will soon be clear, the condition of the magnetic shield turns out to have a rather high impact on the results. We will thus briefly touch upon the method of demagnetizing magnetic shields.

As mentioned in sec.2.5.8 the magnetic shield, used to get rid of as much of any residual magnetic field as possible, consists of several layers of aluminum, iron and mu-metal [25]. Inside the ferromagnetic materials are magnetic domains - communities of atoms - with magnetic moments, and given the freedom of rotational mobility these moments will orient themselves according to any externally applied magnetic field. In the laboratory there are various stray magnetic fields from all sorts of electronic apparatus, not to mention the magnetic field from the earth itself. As for the atomic mobility, however, the magnetic moments are, to some degree, locked in their positions. This can potentially mean that, if the magnetic domains are not oriented in a way as to cancel out the static magnetic background field, it causes a decrease in the quality of magnetic shielding, resulting in higher residual fields inside the shield.

To optimize the effect of the shield we then need to demagnetize (or degauss) the shield. This is done by having wires wound through and around the shield, and then applying a sinusoidal current. The idea is to produce magnetic fields strong enough to release the atomic moments from their orientations and then let them resettle in a configuration that cancels out the magnetic background field - a kind of reshuffling of the magnetic domains. The applied current starts out rather strong (~ 10 A) in order to saturate, and is then slowly decreased.

We will now return to measurements displaying the effect of this demagnetizing process and the interested reader may review [26] for more details on demagnetization. As mentioned above, we now mount our optimized coil configuration inside the magnetic shield and perform MORS measurements like in sec.4.3. As we will see, our limitations on magnetic homogeneity will be defined, not by the magnetic field produced by the coils, but rather by the quality of the magnetic shield.

The data is presented in fig.24. As explained in sec.4.2, for each position of the cell we switch the direction of the current to enable getting rid of the background field in the data processing. For each current direction we get a signal like the one seen in fig.15 where there are two peaks - one for the up-sweep of the frequency sent to the RF-coils and one for the down-sweep. This gives us two estimates of the Larmor frequency for each current direction. Up until now we have taken the mean of those two, but as a sanity check we now want to specifically plot them separately, in order to see to which

degree they agree. As seen in fig.24 they give, for all practical purposes, the same Larmor frequency. Furthermore we see that the change in measured magnetic field strength, ν_L , at different positions along the x -axis (either the red or the green points), is hardly due to inhomogeneity of the produced magnetic field (the black points). It is mainly due to residual background fields, caused by imperfect magnetic shielding. The y -component of the background magnetic field $B_{y,BG}$ corresponds to the difference between the black and the red (or green) points. We see that the variation of $B_{y,BG}$ is clearly larger than the inhomogeneity of the produced field over the 8 cm range $x \in [50, 130]$. The relative standard deviation of the produced field in this range is 2.4‰ which is satisfying, but in reality we cannot get rid of the residual field during a measurement. That is, we would subject our cell to the magnetic profile described by the red (or green) points, which obviously does not fulfill the desired homogeneity.

Thus, to improve the magnetic shielding, we perform the degaussing process, as described above, to the shield. We then conduct the exact same measurement series as presented in fig.24 in order to compare the effect. This data is presented in fig.25. To more easily compare the magnetic profile prior and posterior to deGaussing, the two plots are shown with the same intervals on both axes.

First of all we clearly see the effect in that the red (or green) profile is now much more homogeneous than it was before degaussing. Furthermore we see that the homogeneity of the produced field has now improved as well. This may not be visually obvious from the two plots, but calculations yield that the relative standard deviation in the range $x \in [50, 130]$ has now decreased to 1.1‰.

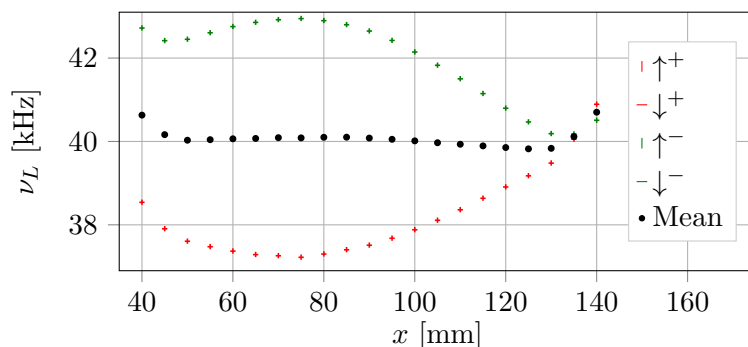


Figure 24: Pre-degaussed MORS measurements of magnetic field inside the shield, produced by the y -coils separated by 51 mm. Relative standard deviation of data points in the 8 cm range $x \in [50, 130]$ is 2.4‰. Arrows indicate up or down-sweep of the RF-frequency while \pm represent the direction of the current applied to the coils.

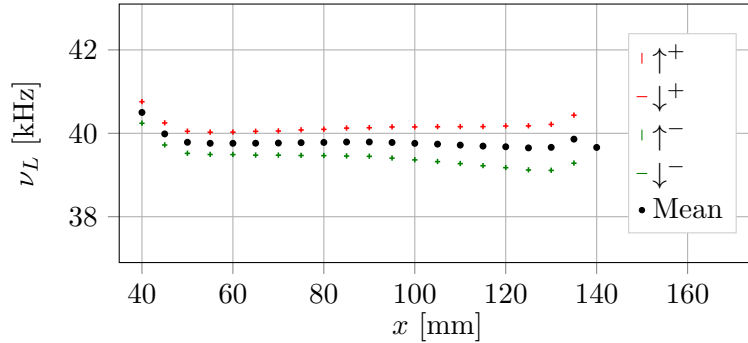


Figure 25: Post-degaussed MORS measurements of magnetic field inside the shield, produced by the y -coils separated by 51 mm. Relative standard deviation of data points in the range $x \in [50, 130]$ is 1.1%. Arrows indicate up or down-sweep while \pm represent direction of current.

We are however still, at least partly, limited by the magnetic shielding. It seems to be the best we can do with the current 'test-shield'. Further improvement of the magnetic environment would therefore include another, better, magnetic shield. Fortunately we have one such shield at our disposal in the QUANTOP laboratories - the so called 'bio-shield'. This shield has, among other things, been used in the biomedical measurements of magnetic fields produced by guinea pig hearts [15] - hence the name. It has more layers than the test-shield and has bigger dimensions which, for our purpose, results in less effect on the magnetic homogeneity from induced magnetization of the shield.

In the process of changing the setup and switching to another magnetic shield we decide to take a few extra steps. As mentioned in sec.1 the primary goal in mind is to combine our setup with a few other experiments. Since we are going to change the setup anyway, we decide to initiate the combination by setting up the bio-shield in the gravitational wave detection (GWD) laboratory. All measurements presented in the rest of this thesis has been conducted using this shield, and a visualization of the setup is seen in fig.51 in appendix C.

4.5 Bio-Shield Coil Characterization

After having installed the bio-shield and mounted all relevant optics, the natural first step is to characterize the magnetic profile produced by the coils in this new experimental configuration. As in sec.4.3 we use a 5 mm cubic cell and conduct a MORS measurement for different positions of the cell.

4.5.1 Bias Coils

We start by characterizing the y -coils. We apply a current of ± 100 mA to the coils and the result of this series of MORS measurements is seen in fig.26. The immediate thing that jumps to the eyes is the obvious out-lier at $x = 100$ mm. Given all previously

obtained magnetic profiles of the y -coils, the validity of this data point may arguably be questioned. It seems in fact that the entire right half of fig.26 is a bit more messy than the left, and we might be able to explain the reason for this. To get these data we need to place the cell at different positions inside a magnetic shield which has end caps on. This means that when the shield is fully assembled one cannot reach the cell. To avoid removing the shield end caps when changing the position of the cell, we mount the cell at the end of a hollow glass cylinder - hollow in order to let the laser propagate freely. At one end of this glass cylinder we mount it to rails while the other end can move freely through a circular holder. Due to physical limitations of the optical table, the length of this glass cylinder is not very long. This results in the cell falling slightly off axis as it approaches the end corresponding to high x in fig.26.

Another thing worth noting is when comparing the magnetic profiles in figs.25 and 26. These two are produced by the exact same coil configuration - the only difference being the magnetic shielding. The latter has a relative standard deviation of measured Larmor frequency of 2.2‰ in the center 8 cm ($x \in [45, 125]$) which renders the magnetic homogeneity in the two plots relatively similar. Yet, they clearly appear different. This has to do with the improvement of the magnetic shield. The inhomogeneity inside the new shield is now primarily caused by inhomogeneity of the magnetic field produced by the coils, not the background. Any further improvement to the magnetic environment would thus lie in optimization of the coils.

It is worth mentioning here that the 2.2‰ has been calculated including the out-lier at $x = 100$ mm. Ignoring this data point the homogeneity becomes 1.8‰. We let fig.26 remain our description of the magnetic profile produced by the y -coils, and carry on to characterizing the z -coils in the new setup.

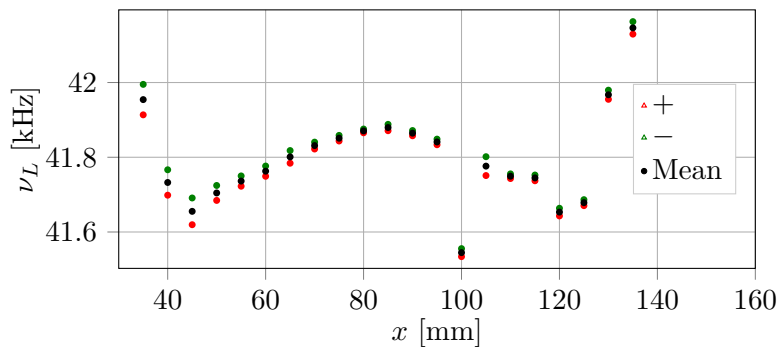


Figure 26: MORS measurements of magnetic field inside the bio-shield, produced by the y -coils separated by 51 mm. \pm represent the direction of the applied current. The relative standard deviation of points in the 8 cm range $x \in [45, 125]$ is 2.2‰ (or 1.8‰ when ignoring the out-lier at $x = 100$ mm).

For this we use the same method as above. We use the z -coils to produce a bias magnetic field and the RF will now be produced by the y -coils. We then conduct a MORS measurement for each position of the 5 mm cubic cell. We apply a current of ± 100 mA,

and the result is seen in fig.27. The first thing to notice is the fact that the background seems to be much bigger at low x -values ⁷ and we have a hypothesis as to why that is. The current source providing the current to the coils is naturally located outside the shield. Wires are thus routed through one of the end caps connecting the coils, and this end corresponds to the left side of fig.27. These wires are twisted around each other so as to minimize the effect on the magnetic field, but the fields from these two wires (in and out) might not be perfectly canceling out one another. The relative standard deviation of the magnetic field in the center 8 cm ($x \in [45, 125]$) is 1.9 ‰ which is again achieving our aim of 3 ‰.

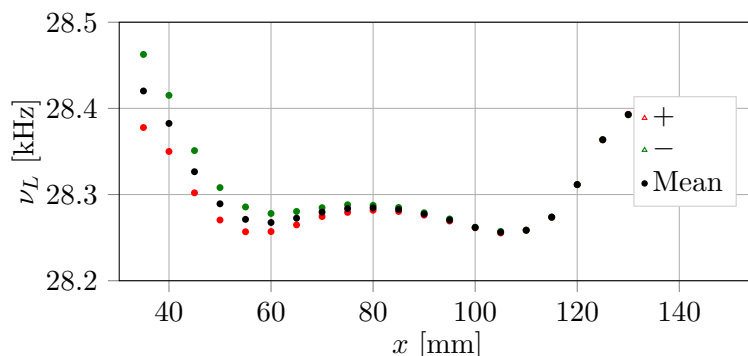


Figure 27: Magnetic profile produced by the z -coils inside the bio-shield. \pm represents the direction of the applied current, and the relative standard deviation of data points in the range $x \in [45, 125]$ is 1.9 ‰

Even though the inhomogeneity of the magnetic profile is primarily caused by the coils, we see in figs.26 and 27 that, even in the bio-shield, we still have some effect from the residual magnetic background field. We do not have a better shield at our disposal, but we may still be able to find a way to manipulate the remaining background field to our advantage. Say for instance that we use the y -coils to create a bias magnetic field. Any spatially independent y -component of the residual magnetic field would thus not effect the homogeneity of the magnetic profile. If, on the other hand, the background is not constant over the center 8 cm (which in reality is more plausible), this would in fact have an effect on the homogeneity. The idea then arises, to produce coils that are specifically designed to create a linear gradient of magnetic field in order to compensate for the inhomogeneity of the residual field - at least to first order. Such compensation coils have been designed for the y and z directions and the coil configuration is then modified to include these as well. A visualization of the complete coil configuration is seen in fig.28. In order to keep all pairs of coils in the desired position we 3D-print a holder in which lines are carved to exactly fit each PCB. The outer, circular dimension of the holder is designed to fit inside the magnetic shield. Furthermore we make an indent in order to make room for wires to go through the shield. These wires will then be used for the

⁷Remember that the background is the difference between the red (or green) and the black points.

degaussing process described in sec.4.4.4.

With the compensation coils now included in the coil configuration we will continue with the characterization of the magnetic fields produced by these coils.

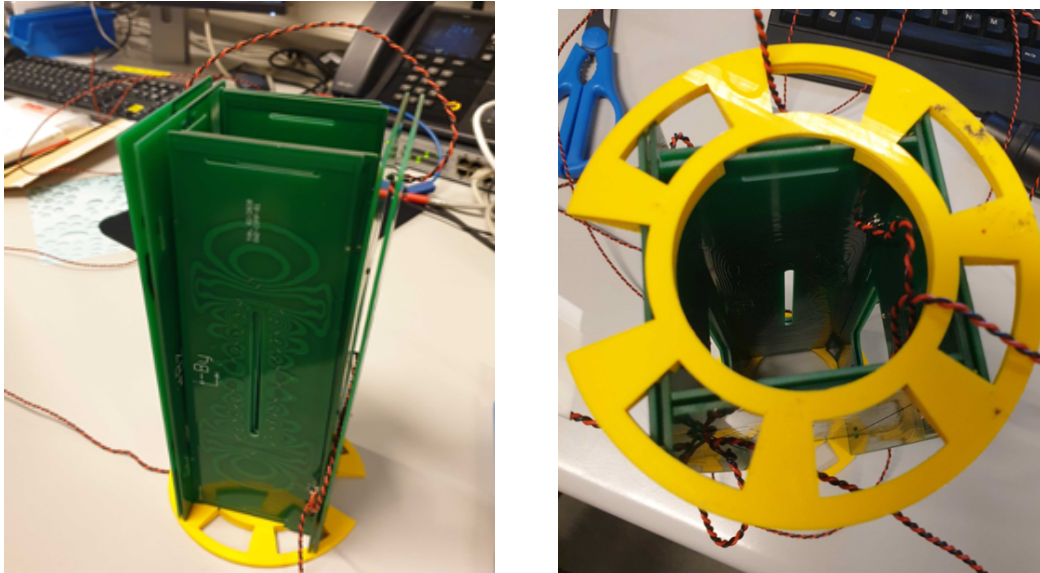


Figure 28: A visualization of the complete coil configuration including both bias -and compensation coils for y and z direction.

4.5.2 Compensation Coils

We start by characterizing the y -compensation coils. However, the procedure used so far needs to be slightly modified. In sec.4.2 we argued why the method of applying \pm current would work. More specifically, to arrive at eq.60 we assumed, practically speaking, that the applied magnetic field needs to be much greater than that of the background. The compensation coils are not designed to produce great magnetic field strengths, merely a small gradient. Furthermore, they are designed to have zero field at the center of the coil system. So as we approach the center, the validity of the above assumption decreases. To cope with this, we apply a bias magnetic field with the y -coils, on top of which we add the gradient field produced by the y -compensation coils. We apply a current of 100 mA to the y -bias coils and ± 100 mA to the y -compensation coils. We then calculate the mean of Larmor frequencies from the \pm current and then subtract this mean from the $+$. This should provide us with a description of the field produced by the compensation coils. The result of this measurement series is seen in fig.29. When inspecting this plot, the reader may wonder how we manage to measure negative Larmor frequencies. It is merely used here to illustrate that the direction of the field produced by the compensation coils has flipped. We see that the magnetic profile fits relatively well with a linear gradient. To acquire a quantitative estimation of the field produced

by the compensation coils we do a linear fit. For this fit procedure we include only the data points in the center 8 cm. The range in which the fit is plotted in fig.29 illustrates which data points have been used.

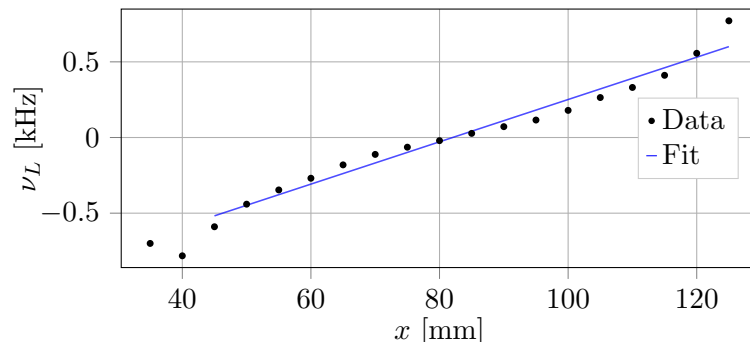


Figure 29: Magnetic field produced by the y -compensation coils inside the bio-shield. An applied current of 100 mA was used, and a linear fit $y = ax + b$ yields a magnetic field gradient of $a = (0.014 \pm 0.01)$ kHz/mm.

We now continue with the characterization of the z -compensation coils. Unfortunately we cannot apply the same method as for the y -compensation coils because there is a short between the z -bias and z -compensation coils. Given that it is rather tedious work to mount the complete coil configuration, together with the vapor cell inside the magnetic shield, we adopt an alternative approach. We compromise the assumption leading to eq.60 and omit applying a bias field with the z -coils. We thus solely apply a \pm current to the z -compensation coils and measure the resulting Larmor frequency. In doing so we bear in mind that data points close to the center (corresponding to $x = 80$ mm in fig.29) may be slightly misleading. The result of this measurement series is seen in fig.30 together with a linear fit plotted in the range illustrating the data points included in the fitting procedure.

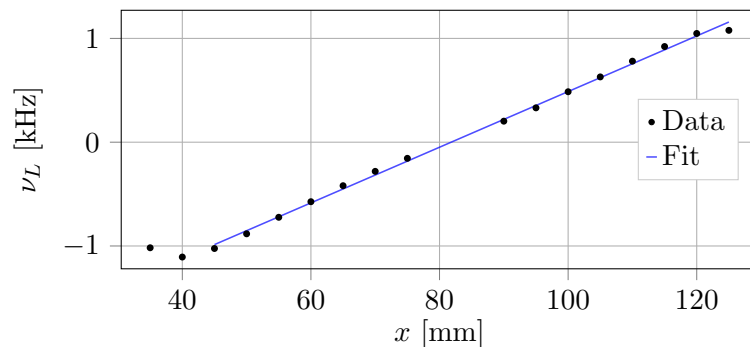


Figure 30: Magnetic profile produced by the z -compensation coils inside the bio-shield. The applied current was 100 mA and a linear fit of the form $y = ax + b$ gives an estimate of the produced magnetic field gradient of $a = (0.027 \pm 0.01)$ kHz/mm.

At this point we conclude all coil characterizations. We have measured, optimized, re-measured and added to the complete coil configuration in order to achieve the best possible magnetic environment. It is now time to switch gears and proceed towards applying this field to a vapor cell with bigger physical dimensions.

5 Long Cell Measurements

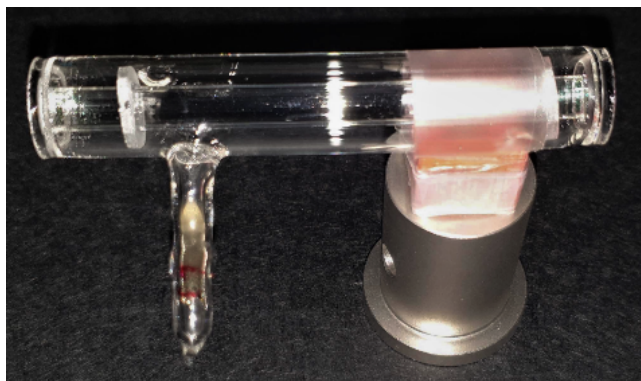


Figure 31: The 8 cm cell (labeled 'L3') is used in all measurements presented in the rest of this thesis. Its total length is 86 mm while each end cap is about 3 mm thick. Total inner dimensions are thus $5 \times 5 \times 80 \text{ mm}^3$.

The cell that will be used for all measurements presented in the rest of this thesis is the one seen in fig.31. It has a total length of 86 mm including the end caps, each having a thickness of about 3 mm. The outer shape is cylindrical, but inside is a square cross section glass tube, each side being 5 mm. The total inner dimensions, in which the atoms are freely moving, are thus $5 \times 5 \times 80 \text{ mm}$.

As mentioned in sec.2.5.8 increasing the size of the vapor cell results in the decreasing of some of the decoherence processes that broadens the MORS signal. The hope now is, that with this long cell subjected to a sufficiently homogeneous magnetic environment, we are able to observe a MORS signal with a much narrower linewidth than say that of a 5 mm cubic cell (which is about 25-30 Hz).

All measurements with the cubic cell have been conducted applying the co-linear MORS method described in sec.2.5.6. Now that we do not have to move the cell around in different positions, but simply place it in the center of the coil configuration, we are able to, at least to some degree, apply the traditional MORS method (sec. 2.5.5). This means that, instead of having only one laser functioning both as a probe and pump, propagating in the x -direction, we can add a laser propagating along the axis of quantization (the y -direction) and use that for pumping. We are thus free to tune the probe laser without this having a big effect on the optical pumping rate. The frequency we choose for the probe is about 3 GHz red detuned from the $6s \ ^2S_{1/2}, F = 4 \rightarrow 6p \ ^2P_{3/2}$ transition. This corresponds to a wavelength of about 852 nm. We then apply a circularly polarized laser beam along the y -axis with a wavelength of about 895 nm corresponding to the $6s \ ^2S_{1/2}, F = 3 \rightarrow 6p \ ^2P_{1/2}, F = 4$ transition (see fig.7).

In a traditional MORS measurement using a 5 mm cubic cell both the probe and pump beams illuminate a relatively big part of the cell. In our case, however, this is only true

for the probe. The waist of the pump beam is roughly 2 mm - not much compared to 8 cm. One may thus wish to spread out this pump beam in order to hit the entire cell, but here we meet other limitations. The hole in the side of the magnetic shield, through which we send the pump beam, has a diameter of about 2 cm. Hence, we are unable to hit most of the cell with the pumping beam.

We choose to do the best possible with the given experimental setup, and mount two planoconvex lenses so as to increase the 'waist' of the pump beam from ~ 2 mm to about 20 mm.

With the setup complete, we are now ready for the first measurement with the long vapor cell, together with the coil system, mounted inside the shield ⁸. We conduct a MORS measurement and fit a Lorentzian to the data. An example of this is seen in fig. 32. One might wonder why we choose to fit a Lorentzian. If we are to observe atoms in the $F = 4$ ground state (see fig.5), eq.49 clearly states that we should see a sum of eight Lorentzians. And the sum of a number of Lorentzians is obviously not necessarily itself a Lorentzian. While this is true, the choice of fitting has to do with the fact that the spacing between the peaks of each of these 8 Lorentzian is negligible compared to their widths. Thus, for all practical purposes, the sum of these is indeed itself a Lorentzian. Now, the two interesting estimates provided to us by such a fit is the central (Larmor) frequency ν_L , and the width Γ_{FWHM} - the latter being the one we wish to make as small as possible.

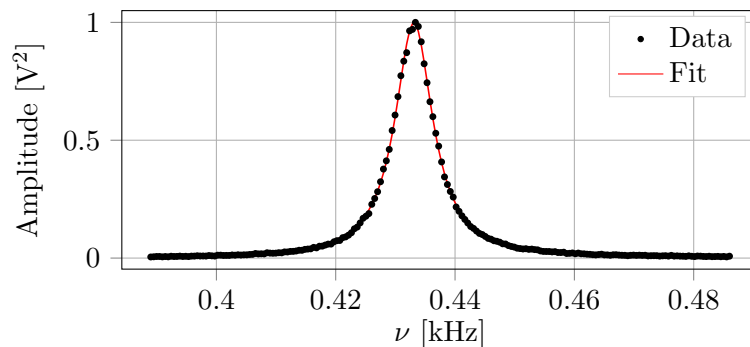


Figure 32: An example of a measured MORS signal with corresponding Lorentzian fit.

5.1 Y-Coils

The first thing we want to investigate is how the width of the MORS signal evolves as a function of applied magnetic field strength. We apply a range of different currents to the y -coils (\pm) and get the width of the signal from a fit as in fig.32. The result of these measurements is seen in fig.33.

Here the negative Larmor frequencies correspond to flipping the direction of the applied current. As expected, the width grows with increasing magnetic field strength. For high

⁸The interested reader may see fig.53 for a visual peak inside the setup

magnetic fields the broadening of the signal is primarily due to magnetic inhomogeneities. For low magnetic fields, however, other decoherence processes have a dominant effect on the width. Fig.33 also includes a second order polynomial fit. We do not necessarily expect the data to follow this function, but the reason for choosing so anyway goes as follows. In [17] it is shown that when applying a magnetic field with a linear gradient, the width as a function of the slope very much follows this form. As seen in fig.26, however, the inhomogeneity of the y -coils used to produce the plot in fig.33 is not a linear gradient. One could argue, though, that each half of this magnetic profile ($x \in [45, 80]$ and $x \in [80, 125]$) is approximately a linear gradient. Even so, the validity of describing the cell as two halves, each with (different) linear gradients, is not particularly clear - we would e.g. neglect the fact that atoms are able to travel from one half to the other. Despite this, the data in fig.33 actually follow the fit rather nicely - especially for high fields. To further explore how the width evolves at low frequencies we would like to collect more data at this low field region and we will do so soon. A final comment on fig.33 is however appropriate. We see at a Larmor frequency of 40 kHz the width is roughly 40 Hz, i.e. the width is about 1‰ of the Larmor frequency. If now we were to extrapolate the data down to low frequencies we could get an idea on how this ratio would behave. The ratio $\Gamma_{\text{FWHM}}/\nu_L$ is plotted in fig.34. We see that it explodes at very low frequencies which is expected since the vapor cell has a natural linewidth even when no magnetic field is present. If, however, we wished to go to Larmor frequencies as low as say 100 Hz and have a ratio of $\Gamma_{\text{FWHM}}/\nu_L = 3‰$ fig.34 shows that we still have obstacles to overcome. We will for now deem this a sufficient description of the performance possible with the given cell and coil system, and continue with an exploration of the effect on the linewidth by the other pairs of coils.

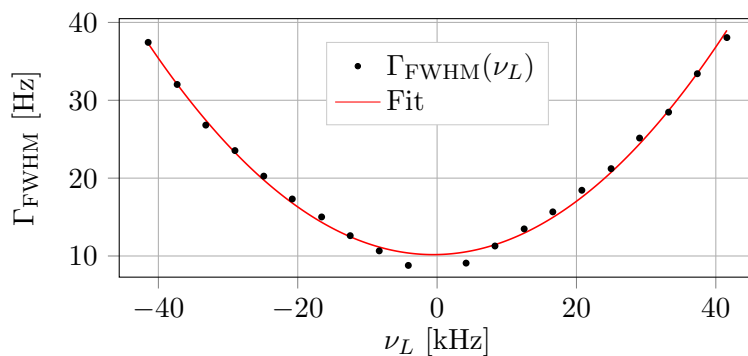


Figure 33: Γ_{FWHM} as a function of Larmor frequency ν_L with corresponding second order polynomial fit. The magnetic fields are produced by the y -coils while both the width and the Larmor frequency are obtained from a Lorentzian fit as in fig.32.

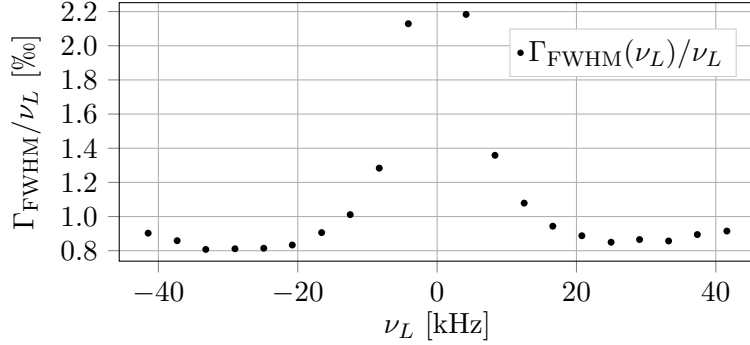


Figure 34: Same data as in fig.33 but now Γ_{FWHM} relative to the corresponding Larmor frequency ν_L , in %.

Prior to all measurements conducted using the 8 cm vapor cell the degaussing procedure (sec.4.4.4) has been performed. This is done in order to minimize the residual magnetic field inside the shield and hence its effect on the linewidth of the MORS signal. There is however still some remaining background magnetic field present. Assuming that this residual field is approximately the same after each degaussing process, we will now attempt to explore to which degree we are able to cancel it out. Granted, we are now entering a somewhat nit-picking domain, regarding the optimization of magnetic environment, but it may be worth examining in order to push the limit of how good a performance, i.e. narrow linewidth, we are capable of achieving.

We start by testing the effect of the y -compensation coils. The idea is to see whether we are able to slightly cancel out the y -component of the background field - or more specifically we will try to cancel out the inhomogeneity of the y -component of the residual background field. In order to be in a magnetic field regime where the background is non-negligible we apply a current of 1 mA to the y -bias coils which corresponds to a Larmor frequency of about 430 Hz. We then send a range of different currents through the y -compensation coils to see how the linewidth of the MORS signal changes. The result is presented in fig.35.

From fig.29 we know that the field produced by the y -compensation coils is approximately a linear gradient, so according to [17] we would expect the linewidth to follow a second order polynomial. But if we were to fit the function $\Gamma_{\text{FWHM}}(I) = aI^2 + bI + c$, the first order term b would be hard to translate into a physical intuition. We fit instead the function $\Gamma_{\text{FWHM}}(I) = a(I - I_0)^2 + c$. In this case I_0 would give an estimate of which current to apply to the y -compensation coils in order to best cancel out the inhomogeneity of the y -component of the residual field. c would then give an estimate of the minimum possible linewidth. From the fit we get $I_0 = (0.87 \pm 0.04)$ mA. For c the fit gives $c = (6.71 \pm 0.39)$ Hz. This indicates that we should be able to reach a linewidth of 6.71 Hz if we were to apply a current of 0.87 mA to the y -compensation coils. The lowest linewidth measured experimentally was 7.7 Hz with an applied current of 502 μ A.

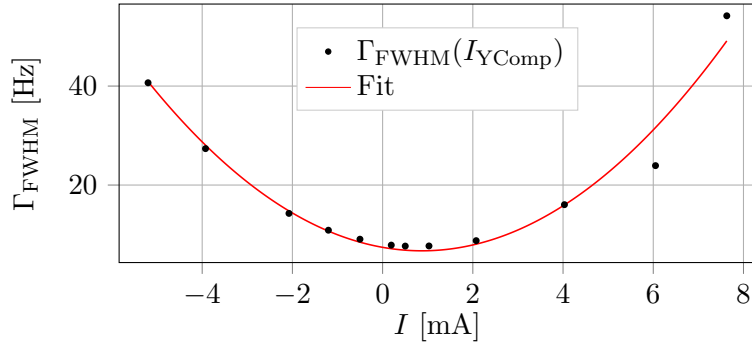


Figure 35: Γ_{FWHM} as a function of applied current to y -compensation coils, while 1 mA is constantly applied to the y -bias coils. A second order polynomial fit of the form $\Gamma(I) = a(I - I_0)^2 + c$ gives the estimates $a = (0.928 \pm 0.019)$ Hz/mA², $I_0 = (0.87 \pm 0.04)$ mA and $c = (6.71 \pm 0.39)$ Hz.

5.2 Z-Coils

Next we move on to the z -bias coils. The idea now is to examine whether we are able to cancel out any constant, i.e. spatially independent, z -component of the background field. We apply a current of 2 mA to the y -bias coils, corresponding to a Larmor frequency of about 850 Hz, and scan over a range of different currents through the z -bias coils to see how the Larmor frequency changes. The result of these measurements is shown in fig.36. As mentioned in sec.4.2 the Larmor frequency is proportional to the total magnetic field strength $|\mathbf{B}|$ which has components in all three cardinal directions. In each of these directions, the magnetic field has contributions from both the background and from the coils. Assuming that the z -bias coils only produce magnetic fields along the z -direction, we then combine the background (BG) fields in the x and y directions with the field produced by the y -bias coils, and fit the data to a function like

$$\nu_L = c \cdot \sqrt{B_{xy} + (B_z + B_{z,\text{BG}})^2} \quad (62)$$

where $B_{xy} = B_{x,\text{BG}}^2 + (B_{y,\text{bias}} + B_{y,\text{BG}})^2$, $B_{z,\text{BG}}$ is background along z and B_z is the field produced by the coils. The reason for the small disagreement at the lower left part of fig.36 is probably due to the fact that the vapor cell stretches over several centimeters. At any given point along the cell the z -component of the background field is canceled out when some specific current in the 3 mA range in fig.36 is applied to the z -bias coils. But this may not be, in fact it most certainly is not, the same current at every position. And since we exploit the entire cell when conducting a measurement we will see some mix from atoms located at different parts of the cell. The background field in the z -direction $B_{z,\text{BG}}$ is estimated from the fit to be $B_{z,\text{BG}} = (-0.025 \pm 1.030)$ mA. It may seem illogic to measure magnetic fields in units of mA, but we are essentially not interested in the exact magnetic field strength, rather the corresponding current to apply to the coils. Furthermore, the error on $B_{z,\text{BG}}$ is huge, so we conclude that whatever z -component of

the residual field may be present, we are not able to cancel it out by the means of our z -bias coils.

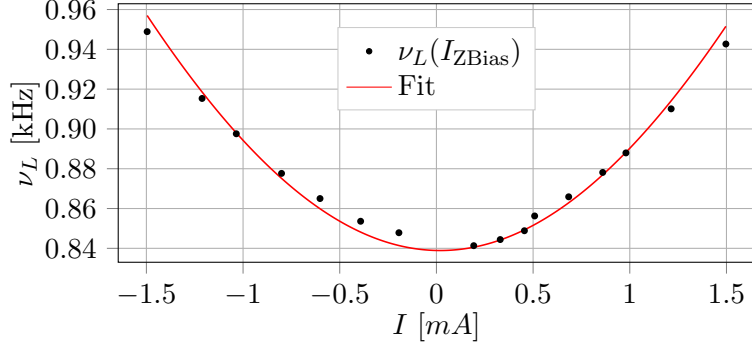


Figure 36: ν_L as a function of current applied to the z -coils while constantly running 2 mA through the y -coils for bias magnetic field. The fit function $\nu_L = c \cdot \sqrt{B_{xy} + (B_z + B_{z,BG})^2}$ yields the estimates $c = 0.293 \pm 0.623$, $B_{xy,BG} = 8.217 \pm 12.642$ and $B_{z,BG} = -0.025 \pm 1.030$.

We will end this section by investigating whether we are able to cancel out any gradient of the z -component of the residual field. We apply a current of about 2 mA to the y -bias coils, corresponding to a Larmor frequency of roughly 850 Hz. We then scan through a range of currents to apply to the z -compensation coils and observe how the linewidth of the MORS signal evolves. The result is presented in fig.37. We fit the data to a function of the form $\Gamma_{FWHM}(I) = a(I - I_0)^2 + c$, given that the magnetic profile produced by the z -compensation coils is quite linear, as seen in fig.30. From the fit we get the estimate $I_0 = (-0.28 \pm 0.87)$ mA. This should give us an idea of what current to send through the coils in order to best cancel out any gradient of the background z -component, but given the uncertainty this is obviously a rough estimate. We may thus conclude that we are not able to make the magnetic fields along z more homogeneous by the means of the z -compensation coils. More accurate is the fit parameter $c = (8.12 \pm 0.24)$ Hz. This should give an idea about which linewidth to expect without any contribution from inhomogeneity of magnetic fields along z . We see again that a linewidth of about 8 Hz seems to be the lower limit.

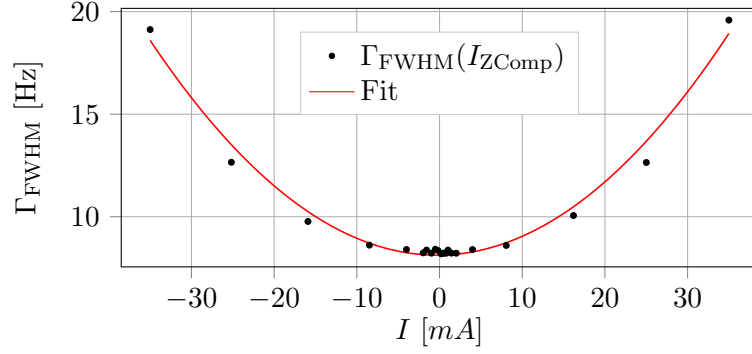


Figure 37: Γ_{FWHM} as a function of current applied to the z -compensation coils while constantly running 2 mA through the y -bias coils. A fit of the form $f(x) = a(x - x_0)^2 + c$ yields the estimates $a = (8.69 \pm 0.57) \cdot 10^{-3} \text{ Hz/mA}^2$, $x_0 = (-0.28 \pm 0.87) \text{ mA}$ and $c = (8.12 \pm 0.24) \text{ Hz}$.

We now conclude this part of our explorations, and continue towards a measuring method more related to what will be utilized in the detection of gravitational waves.

6 Noise Measurements

In this section we adjust our technique, and attempt to observe quantum mechanical noise of an atomic ensemble. This is a step towards the approach that will eventually be applied in GWD, and may be considered a preliminary exploration into parts of the underlying mechanisms behind such a scheme.

The feature we exploit is that a quantum mechanical state of an atom is disturbed by its interaction with the environment. This environment may be comprised of several different sources which all contribute to the disturbance of the atomic quantum state. When measuring the states of the atoms we use light, and in this process the disturbance of atomic states leads to noise in the outgoing signal - that is, light carries information about the (disturbed) state of the atoms.

Our setup is again surrounding the long $5 \times 5 \times 80 \text{ mm}^3$ atomic vapor cell. We apply a bias magnetic field via our y -bias coils, but we now omit the RF-field inducing magnetic transitions as in the MORS measuring scheme. We optically pump the atoms along the y -direction with a circularly polarized pump beam resonant with the $^2\text{S}_{1/2}$, $F = 3 \rightarrow 6\text{p } ^2\text{P}_{1/2}$, $F = 4$ transition, and apply a probe beam 3GHz red detuned from the $6\text{s } ^2\text{S}_{1/2}$, $F = 4 \rightarrow 6\text{p } ^2\text{P}_{3/2}$ transition along the x -direction. After interacting with the atoms, the probe beam travels to a balanced detector, from where the signal is sent through a spectrum analyzer in order to acquire the power spectral density (PSD). For each measurement we take the average of about 500 PSDs.

From [17] we get a mathematical formulation of the spectrum $\Phi(\omega)$ given by

$$\Phi(\omega) = \frac{S_y}{2} \epsilon_z + \frac{\frac{1}{4} a^2 S_y^2}{(\omega_L - \omega)^2 + \Gamma^2} \left[\frac{a^2 J_y^2 S_y \epsilon_x}{2} + 2\Gamma |J_y| \right] + \text{neg.freq.} \quad (63)$$

Let us go through all parameters in eq.63. S_y is the Stokes operator describing the polarization of light as presented in sec.2.5.3, and $\epsilon_{z,x}$ are squeezing parameters. In our case we use a coherent (vacuum) state for the probe beam, so we set $\epsilon_z = \epsilon_x = 1$. a is the coupling strength for the atom-light interaction, ω_L the Larmor frequency and Γ (HWHM) describes the broadening due to decoherence processes. Finally J_y describes the collective spin state of the atomic ensemble (see sec.2.3). It is appropriate here to note that in the derivation of eq.63 the narrow band approximation $\Gamma \ll \omega_L$ and $|\omega_L - \omega| \ll \omega_L$ has been made.

The interpretation of eq.63 is relatively straightforward. The first term is the noise from the probe laser. In our case this gives the shot noise level (SNL) which in a PSD is just an offset - i.e. white noise. In front of the brackets is a Lorentzian that peaks at the Larmor frequency $\omega = \omega_L$. Inside the brackets we have two terms, the first of which represents the noise from quantum back action (QBA). It originates from the quantum fluctuations of the probe beam affecting the atomic spin state. The last term inside the brackets is called projection noise and describes the intrinsic quantum fluctuations of the spin state.

Now, by integrating over frequencies we can find the back action noise area (BANA) and the projection noise area (PNA) given by

$$\text{BANA} = \frac{\pi a^4 J_y^2}{\Gamma} \left(\frac{S_y}{2} \right)^3, \quad \text{PNA} = 2\pi a^2 |J_y| \left(\frac{S_y}{2} \right)^2. \quad (64)$$

We see that these scale differently with both photon flux S_y and spin size J_y . Additionally we have a relation between the PNA, the BANA and the shot noise level (SNL) given by

$$\text{PNA} = 2\sqrt{\pi\Gamma(\text{BANA}) \cdot (\text{SNL})}. \quad (65)$$

Other contributions to the noise area is expressed by the technical noise area (TNA). The total area A ⁹ of the PSD thus becomes

$$A \equiv \text{BANA} + \text{PNA} + \text{TNA}. \quad (66)$$

With the theory above at hand, we are now ready to initiate experimental explorations of these phenomena. For all noise measurements conducted, we first measure the electronic noise of the detectors etc. - that is, without any probe beam. From this data we get an estimate of the amplitude of the electronic noise, specifically in the frequency region of interest. Having acquired the data from a noise measurement, this level of electronic noise is then subtracted from the data. For each measurement the data is normalized to shot noise level, and then fitted to a Lorentzian of the form

$$\Phi(\nu) = a \frac{(\Gamma/2)^2}{(\nu - \nu_L)^2 + (\Gamma/2)^2} \quad (67)$$

so that a gives the amplitude at resonance ($\nu = \nu_L$)¹⁰. Note that the amplitude a in eq.67 should not be confused with the coupling strength a in eqs.63 and 64 - the latter having been absorbed into the former. An example of raw data, together with the corresponding level of electronic noise is seen in fig.38.

⁹When the shot noise has been subtracted.

¹⁰Note here that Γ is FWHM.

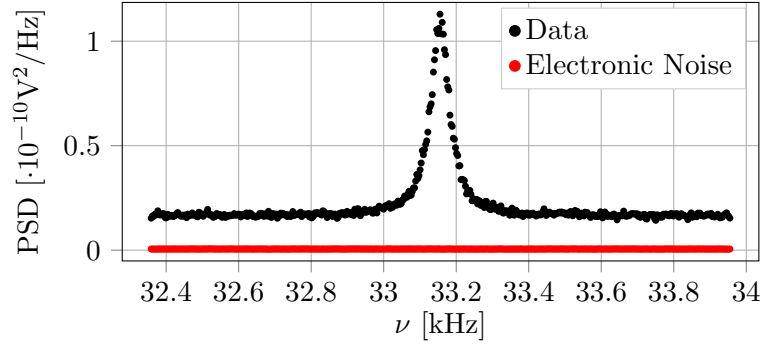


Figure 38: An example of a PSD measurement. The red points are electronic noise measured prior to applying the probe beam.

6.1 Different Larmor Frequencies

We begin by acquiring a PSD for different Larmor frequencies by applying a range of different currents to the y -bias coils. From the Lorentzian fit (eq.67) we get both an amplitude a and a linewidth Γ together with the Larmor frequency ν_L . Fig.39 shows the amplitude as a function of Larmor frequency. As expected we see an increase of amplitude for lower frequencies. As we saw in secs.4 and 5 the inhomogeneity of the applied magnetic field broadens the signal. For decreasing ν_L we get less broadening resulting in an increase in amplitude.

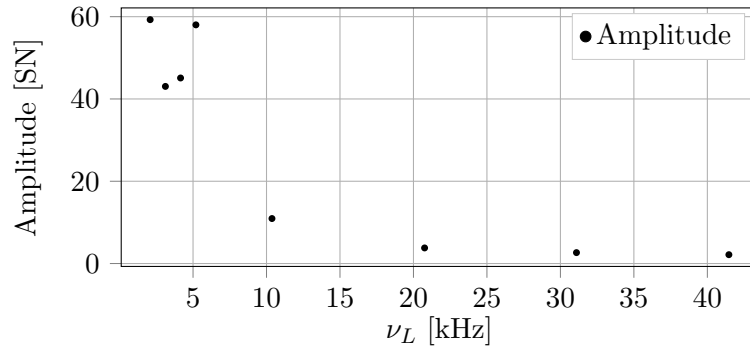


Figure 39: Amplitude (a in eq.67) as a function of Larmor frequency. a ranges from 2.2 at $\nu_L = 41.5$ kHz to 59.3 at $\nu_L = 2.1$ kHz.

We are however able to extract even more information from the fit. By integrating eq.67 we get

$$\int_{-\infty}^{\infty} a \frac{(\Gamma/2)^2}{(\nu - \nu_L)^2 + (\Gamma/2)^2} d\nu = \frac{\pi a}{2\Gamma}. \quad (68)$$

We thus have an estimate of the area described in eq.66. For the data show in fig.39 the corresponding area is plotted in fig.40. Now, these two plots appear quite similar in

shape, which is actually not at all trivial. From eqs.64 we see that neither BANA nor PNA depends on the Larmor frequency. This in itself, together with eq.66 implies that the added contribution to the area for low ν_L must come from classical sources - i.e. we observe increased technical noise at lower Larmor frequencies. We may however be aware to look before we leap. We also see from eqs.64 that BANA is inversely proportional to the linewidth, which we know decreases for lower ν_L . If we now go back to sec.5.1 and revisit fig.33 we see that, in the range $\nu_L \sim 4$ kHz to $\nu_L \sim 41$ kHz, the linewidth changes by a factor of about 4. Comparing this to fig.40 where, in the same range, we have an increase of area by a factor of about 50, we conclude that the increase in area for low frequencies is indeed primarily due to an increased level of technical noise.

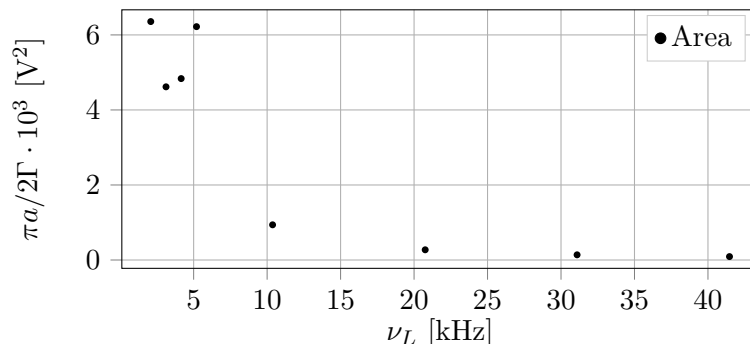


Figure 40: Area (eq.68) as a function of Larmor frequency ranges from $A = 0.09$ at $\nu_L = 41$ kHz to $A = 6.3$ at $\nu_L = 2$ kHz.

Finally we explore how the linewidth changes with Larmor frequency. The data is presented in fig.41. Now, this is a measurement very similar to the one shown in fig.33, the only difference being the measuring method. Comparing the two figures we see that for higher Larmor frequencies the linewidths are relatively similar, but for lower Larmor frequencies, the noise measurement has more broadening than does the MORS measurement. This may be due to the fact that when performing a MORS measurement we apply also the RF-field resulting in a higher signal - or rather bigger signal-to-noise ratio. Whereas we, when using the MORS method, were able to achieve a linewidth of ~ 8 Hz, for the noise measurements the lowest measured linewidth is ~ 15 Hz. Note here the peculiarity of the four data points with the lowest Larmor frequencies in fig.41. By mere visual inspection, these data points seem to be equal. While their values are very close, they are in fact not exactly the same. One explanation for this follows the same reasoning as for the measurement presented in fig.36. Magnetic inhomogeneities contribute to the broadening, and at higher Larmor frequencies, i.e. stronger magnetic fields, this broadening is primarily due to imperfections of the applied magnetic field. At lower Larmor frequencies, the inhomogeneity of the background field becomes more significant. At this regime the two fields (applied and background) compete. While this may not entirely explain the peculiarity seen in fig.41, we would expect it to cause a mismatch in linewidth for lower compared to higher Larmor frequencies. Another explanation for

why these lower frequency data points behave this way, may be due to power broadening of the probe over-shadowing the broadening from magnetic inhomogeneities. However, for the measurements shown in fig.41 the applied probe power was $1.8 \mu\text{W}$ and as will be clear in sec.6.2 this effect should be negligible.

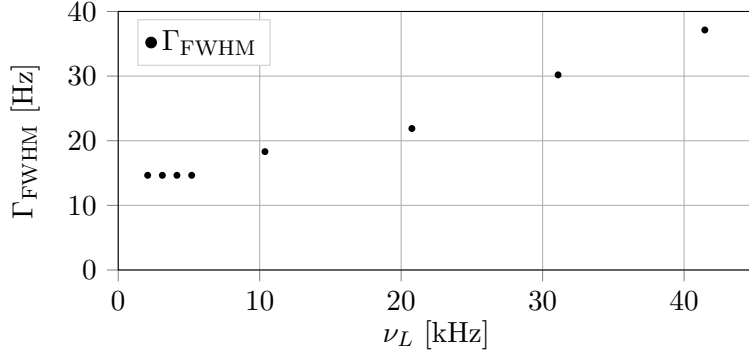


Figure 41: Γ_{FWHM} as a function of Larmor frequency. Comparing with fig.36, the linewidths for higher Larmor frequencies agree very well, but for lower frequencies we now have an increase in linewidth of a factor of about two. Be aware that the four data points with lowest Larmor frequencies are in fact different.

6.2 Changing Probe Power

We now turn to a series of measurements exploring how the PSD evolves with different probe powers. We send a constant current of 75 mA through the y -bias coil, corresponding to a Larmor frequency of about 33 kHz, and apply different powers to the probe beam in the range 0.4-13 mW. We repeat the procedure in sec.6.1 by subtracting electronic noise, normalizing to shot noise and fit eq.67. A plot of the amplitude as a function of probe power is seen in fig.42. As presented in [7] we would expect a linear dependence for low probe powers and then an asymptotic approach to some arbitrary value. One could argue that it is linear for probe powers < 2 mW, but for higher probe powers we clearly see a decrease in amplitude. One explanation for this has to do with the fact that the amplitude has been normalized to the shot noise level. For all data points in fig.42 we pick out a range of ± 1 kHz around the resonance frequency. After removing the Larmor peak, we use the remaining data points to estimate the shot noise level. Now, fig.43 shows the PSD in the range $\nu \in [0, 60]$ kHz, from the measurement where the probe power was 7 mW. We see the Larmor peak at 33 kHz in an otherwise flat region. Fig.44, on the other hand, shows the PSD in the same range for the measurement with a probe power of 13.3 mW. Here we clearly see that the Larmor peak ($\nu_L = 33$ kHz) sits on top of an emerging broadband noise. This shows that the estimation of the shot noise level for a probe power of 13.3 mW, corresponding to the rightmost data point in fig.42, becomes too high. By investigating fig.44 we conclude that this gives a factor of about two. We may thus multiply the rightmost data point in fig.42 by a factor of two, in order to correct for a misleading estimation of the corresponding shot noise level. Whether

we can apply the same reasoning to the measurement shown in fig.43 is not completely obvious, and it seems however that we still have a slight decrease in amplitude for higher probe powers.

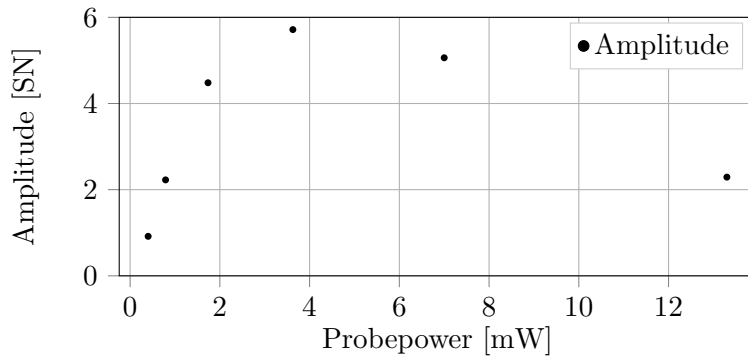


Figure 42: Amplitude (a in eq.67) as a function of probe power.

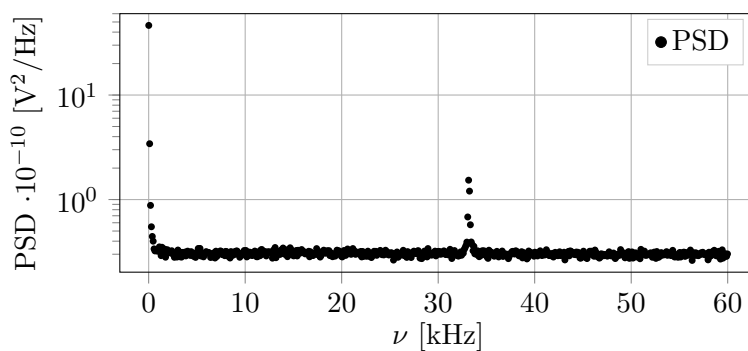


Figure 43: PSD for a probe power of 7 mW. We see the resonance response at $\nu = 33$ kHz.

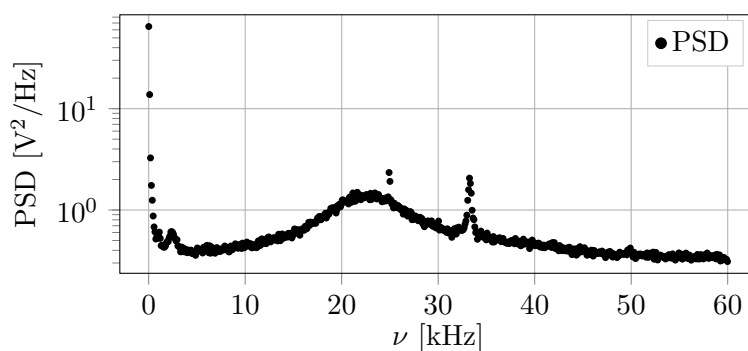


Figure 44: PSD for a probe power of 13.3 mW. Note that the Larmor peak at $\nu = 33$ kHz sits on top of an emerging broadband noise peak.

Finally we investigate how the linewidth changes with changing probe powers. This is depicted in fig.45. In [20] it is shown that we would expect a dependence of a second order polynomial. Different processes contribute to the power broadening, such like an inhomogeneous intensity distribution from the probe over the cross section of the vapor cell. We have left out a polynomial fit to the data, given the fact that we would not (yet) be able to distinguish the individual contributions from one another.

The final goal would thus be to minimize all contributions to the noise except for back action. Or, since we cannot get rid of projection noise, a more precise formulation would be to maximize the back-action-to-projection-noise ratio where the latter includes classical noise.

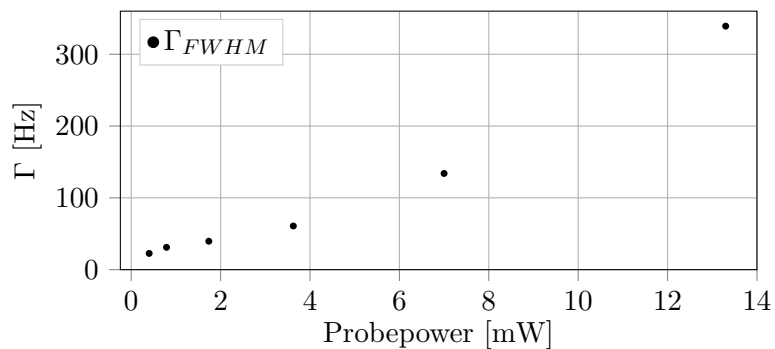


Figure 45: Linewidth Γ_{FWHM} as a function of probe power.

7 Discussion

We devote this final chapter to a few remarks on the results of our efforts. We then, retrospectively, discuss how further improvements could have been achieved and discuss suggestions on future explorations.

7.1 Conclusion

In this thesis we have presented a brief view of the part of general relativity from which the idea of gravitational waves originates. We examined the basic theory behind optical magnetometry together with the mechanisms underlying the process of preparing atomic quantum states by optical pumping schemes.

We then explained the essentials of the technique we used to design PCBs that constitute a coil system. We have characterized the magnetic field produced by the coils and optimized the configuration in order to increase the magnetic homogeneity. We obtained a magnetic homogeneity with a relative standard deviation of 1.1 % over 8 cm.

We then applied the produced magnetic field to a $5 \times 5 \times 80 \text{ mm}^3$ atomic vapor cell and investigated to which degree we were able to cancel out the inhomogeneity of the residual magnetic field. Experimentally we measured a MORS signal with a linewidth as low as $(7.7 \pm 0.5) \text{ Hz}$ at a Larmor frequency of $\nu_L = 433 \text{ Hz}$. Comparing to [16], where measurements were conducted using the same cell, the smallest measured linewidth was 16.32 Hz. The results presented in this thesis suggest that this was not limited by the natural linewidth of the cell. Furthermore, this 16.32 Hz linewidth was measured without any externally applied magnetic field - i.e. the only magnetic field being from the background. When applying a magnetic field, the signal was simply too weak (broadened), suggesting that the applied field was too inhomogeneous for any usage of long cells.

Finally we presented a preliminary exploration into the procedure of directly measuring the atomic noise of a spin ensemble, at quantum levels.

7.2 Outlook

As for most ventures, the process of obtaining the results presented throughout this thesis has endowed us with additional knowledge. Unpredicted challenges often bring with them valuable experience, and the experimental work in this thesis has been no exception.

Regarding the design of our coils system, there are two primary suggestions on further improvement. Firstly, as mentioned in sec.3.2, we ignored the effect of the magnetic shield on the produced magnetic field due to induced magnetization. In appendix A we present the theory on how to include this effect, and with a sufficient level of computational skills this may enable us to design a coil system that produces magnetic fields with even better homogeneity. Secondly, we could reflect on which Larmor frequencies are of interest. The innermost layer of the magnetic shield is made of aluminum and shields against high frequency magnetic fields ¹¹. Since this shield defines the limits on the

¹¹On the order of MHz.

physical size of our coil system, we may benefit from removing this shield entirely from the setup, thus enabling the design of an enlarged version of the coil system, assuming this would increase the magnetic homogeneity.

The long cell shown in fig.31 is only one of several, and prior to the fabrication of the coil system presented in this thesis, no method has been available to characterize the performance of these long cells. This would be an interesting assignment to take on in the near future, but it comes with several other speculations. As explained in sec.2.5.7 there are different decoherence processes that effect the linewidth of a signal, such like magnetic inhomogeneity, but also phenomena like atom-atom collisions and atom-wall collisions. The linewidth observed is a sum of all these processes and further improvement contains estimations of the individual contributions, which requires computational simulations. Such a task has recently been undertaken at QUANTOP, and this is definitely another suggestion on explorations to do in the coming months.

A final remark in relation to the vapor cells has to do with optical pumping. As explained in Chapter 5 we have only been covering about a quarter of the vapor cell, which results in a smaller pumping rate - i.e. a decrease in spin polarization. If we were able to hit the entire cell with both pump and repump beams, this would improve the detected signal. We have a few ideas on how to do this, including a series of beam splitters or a system of lenses. Whatever method will be chosen, this is an essential part of future improvements to the setup.

Finally, in order to make the setup applicable to GWDs we need to combine it with the experiment that uses parametric down conversion to create entangled beams. This will be the crown of our efforts, and only the future will know what new observations may await.

7.3 Acknowledgments

I would like to finish this thesis by paying my gratitude to all who have given their support and assistance through the past eighteen months.

Special thanks to Professor Eugene Polzik for giving me the opportunity to do my thesis at QUANTOP. In particular I appreciate your occasionally unusual honesty.

Huge thanks to my supervisor Michael Zugenmaier for your extraordinary pleasant company and patient guidance. You are the essence of an excellent sparring partner.

Thanks to Rodrigo Thomas for your warm-hearted presence and for always taking your time to discuss, explain and educate.

Also, thanks to Jun Jia for sharing your everlasting train of thoughts, and for creating an enjoyable working environment.

To Jürgen Appel for taking your time to answer questions on your script, despite having found a job outside QUANTOP.

To Associate Professor Jörg H. Müller for being an exceptional educator.

And finally thanks to the rest of the QUANTOP group for creating an adept and relaxing atmosphere.

References

- [1] <https://physics.nist.gov/PhysRefData/Handbook/Tables/cesiumtable1.htm>.
- [2] <https://steck.us/alkalidata>.
- [3] Electronic components. <https://www.digikey.dk/products/en>.
- [4] Ligo research and development. <https://www.ligo.caltech.edu/WA/page/research-development>.
- [5] News & press releases. <http://www.ligo.org>.
- [6] Pcb prototype and pcb fabrication manufacturer. <https://jlcpcb.com>.
- [7] Rodrigo A. *Optical spin-mechanics quantum interface*. PhD thesis, 2020.
- [8] Kenneth Barbalace. Periodic table of elements. <https://environmentalchemistry.com/yogi/periodic/Cs.html>.
- [9] Thorsten Bæk and Ryan Yde. *Optical magnetometry*, 2018.
- [10] Christopher J. Foot. *Atomic physics*. Oxford Univ. Press, 2011.
- [11] Bosch Global. Bno055, Jun 2020. <https://www.bosch-sensortec.com/products/smart-sensors/bno055.html>.
- [12] David J. Griffiths. *Introduction to quantum mechanics*. Pearson, 2014.
- [13] David Jeffrey Griffiths. *Introduction to electrodynamics*. Prentice Hall, 3 edition, 1999.
- [14] Troels Harmark. *General relativity and cosmology*, 2019. Lecture notes.
- [15] Kasper Jensen, Rima Budvytyte, Rodrigo A. Thomas, Tian Wang, Annette M. Fuchs, Mikhail V. Balabas, Georgios Vasilakis, Lars D. Mosgaard, Hans C. Stærkind, Jörg H. Müller, and et al. Non-invasive detection of animal nerve impulses with an atomic magnetometer operating near quantum limited sensitivity. *Scientific Reports*, 6(1), 2016.
- [16] Mathias J.R. Effect of inhomogeneous magnetic fields on mors signal for long cells (8cm), Aug 2018. Summer Project.
- [17] Brian Julsgaard. *Entanglement and Quantum Interactions with Macroscopic Gas Samples*. PhD thesis, 2003.
- [18] Farid Y. Khalili and Eugene S. Polzik. Overcoming the standard quantum limit in gravitational wave detectors using spin systems with a negative effective mass. *Physical Review Letters*, 121(3), 2018.

- [19] Joseph L. Kirschvink. Uniform magnetic fields and double-wrapped coil systems: Improved techniques for the design of bioelectromagnetic experiments. *Bioelectromagnetics*, 13(5):401–411, 1992.
- [20] Hanna Krauter. *Generation and application of entanglement of room temperature ensembles of atoms*. PhD thesis, 2011.
- [21] Christoffer B. Møller, Rodrigo A. Thomas, Georgios Vasilakis, Emil Zeuthen, Yeghishe Tsaturyan, Mikhail Balabas, Kasper Jensen, Albert Schliesser, Klemens Hammerer, Eugene S. Polzik, and et al. Quantum back-action-evading measurement of motion in a negative mass reference frame. *Nature*, 547(7662):191–195, 2017.
- [22] Christoffer Bo Møller. *Quantum Back-Action Evasion in a Hybrid Spin-Optomechanics System*. PhD thesis, 2018.
- [23] Christian Anker Rosiek. Project outside of course scope, Nov 2018.
- [24] S. J. Seltzer, M. A. Bouchiat, and M. V. Balabas. Surface coatings for atomic magnetometry. *Optical Magnetometry*, page 205–224.
- [25] Hans Chr. Stærkind. Optical magnetometry for biomedical applications, 2016.
- [26] F. Thiel, A. Schnabel, S. Knappe-Grüneberg, D. Stollfuß, and M. Burghoff. De-magnetization of magnetically shielded rooms. *Review of Scientific Instruments*, 78(3):035106, 2007.
- [27] Gordon Kemble. Woodgate. *Elementary atomic structure*. University Press, 1980.
- [28] Qingyun Zeng. The laplace equation on a solid cylinder. <https://www.math.upenn.edu/~qze/math241s17/laplacecylinder-3.pdf>.
- [29] Emil Zeuthen, Eugene S. Polzik, and Farid Y. Khalili. Gravitational wave detection beyond the standard quantum limit using a negative-mass spin system and virtual rigidity. *Physical Review D*, 100(6), 2019.

Appendices

A Including Induced Magnetization

Here we present the theory on how to implement the effect from the magnetic shield, on the produced magnetic field, in the calculations of the PCB traces.

We begin with Maxwell's equations

$$\nabla \cdot \mathbf{E} = \rho/\epsilon_0 \qquad \nabla \cdot \mathbf{D} = \rho \qquad \text{(I)}$$

$$\nabla \cdot \mathbf{B} = 0 \qquad \nabla \cdot \mathbf{B} = 0 \qquad \text{(II)}$$

$$\nabla \times \mathbf{E} = -\partial\mathbf{B}/\partial t \qquad \nabla \times \mathbf{E} = -\partial\mathbf{B}/\partial t \qquad \text{(III)}$$

$$\nabla \times \mathbf{B} = \mu_0\mathbf{j} + \mu_0\epsilon_0\partial\mathbf{E}/\partial t \qquad \nabla \times \mathbf{H} = \mathbf{j} + \partial\mathbf{D}/\partial t \qquad \text{(IV)}$$

In vacuum

In matter

with constitutive relations (in a linear media)

$$\mathbf{D} = \epsilon\mathbf{E} \quad , \quad \mathbf{B} = \mu\mathbf{H}. \qquad \text{(69)}$$

The magnetic field inside the shield originates from the currents directly \mathbf{B}_I , and the induced magnetization of the shield \mathbf{B}_m , so

$$\mathbf{B} = \mathbf{B}_I + \mathbf{B}_m. \qquad \text{(70)}$$

From (IV) we get

$$\nabla \times \mathbf{B} = \nabla \times \mathbf{B}_I + \nabla \times \mathbf{B}_m = \mu_0\mathbf{j}. \qquad \text{(71)}$$

Thus

$$\nabla \times \mathbf{B}_m = 0. \qquad \text{(72)}$$

From vector identities we know that the curl of the gradient of any scalar field is zero, and we can therefore find a scalar potential ψ (on the shield), such that $\mathbf{B}_m = -\nabla\psi$.

From (I) it follows that

$$\nabla \cdot \mathbf{B} = \nabla \cdot (-\nabla\psi) = \nabla^2\psi = 0 \qquad \text{(73)}$$

i.e. ψ solves the Laplace equation.

Let us now remind ourselves of the geometry presented in [sec.3.2](#)

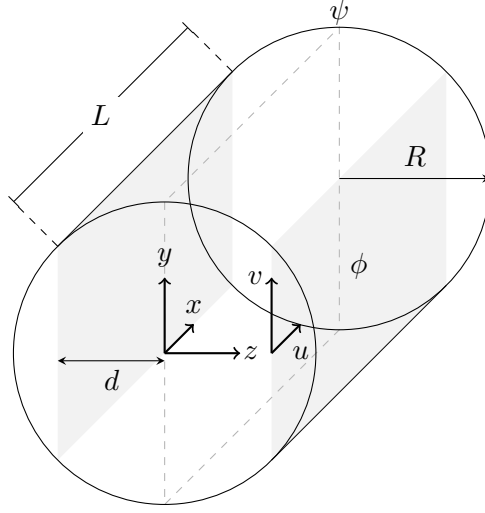


Figure 47: Current sheets inside a cylindrical magnetic shield.

where we have now included the scalar potential ψ on the surface of the shield. The two current sheets, illustrated by the gray areas, have local coordinates (u, v, d) and $(u, v, -d)$ and current density

$$\mathbf{j} = \nabla_{uvd} \times \begin{pmatrix} 0 \\ 0 \\ \phi(u, v) \end{pmatrix} \cdot (\delta(z-d) + \delta(z+d)) = \begin{pmatrix} \partial_v \phi \\ -\partial_u \phi \\ 0 \end{pmatrix} \cdot (\delta(z-d) + \delta(z+d)) \quad (74)$$

From Biot-Savart's law we get

$$\mathbf{B}_I = \frac{\mu_0}{4\pi} \iiint \frac{\mathbf{j} \times (\mathbf{r} - \mathbf{r}')}{|\mathbf{r} - \mathbf{r}'|^3} d^3\mathbf{r}' = \frac{\mu_0}{4\pi} \sum_{d'=\pm z} \iint \frac{\begin{pmatrix} \partial_v \phi \\ -\partial_u \phi \\ 0 \end{pmatrix} \times \begin{pmatrix} x-u \\ y-v \\ z-d' \end{pmatrix}}{\left| \begin{pmatrix} x-u \\ y-v \\ z-d' \end{pmatrix} \right|^3} dudv \quad (75)$$

If we now assume a shield with $\mu \rightarrow \infty$, then at the air-shield interface the magnetic field is normal to the shield surface $\mathbf{B} \parallel \mathbf{n}$, i.e. $\mathbf{B} \cdot d\mathbf{s} = 0$ for all tangential $d\mathbf{s}$.

Thus

$$0 = \mathbf{B} \cdot d\mathbf{s} = \mathbf{B}_I \cdot d\mathbf{s} + \mathbf{B}_m \cdot d\mathbf{s} = \mathbf{B}_I \cdot d\mathbf{s} - (\nabla\psi) \cdot d\mathbf{s}. \quad (76)$$

By integrating along a closed path $\partial\Omega$ enclosing an area Ω on the surface of the shield we get

$$\oint_{\partial\Omega} (\nabla\psi) \cdot d\mathbf{s} = \oint_{\partial\Omega} \mathbf{B}_I \cdot d\mathbf{s} \quad (77)$$

Invoking Stokes' theorem to the right hand side of eq.77 we get

$$\oint_{\partial\Omega} \mathbf{B}_I \cdot d\mathbf{s} = \iint_{\Omega} (\nabla \times \mathbf{B}_I) \cdot d\mathbf{n} = \iint_{\Omega} \mu_0 \mathbf{j} \cdot d\mathbf{n} = 0 \quad (78)$$

where the last equality is due to no current crossing the interface. Since eq.78 holds for any given path $\partial\Omega$ we get the left hand side of eq.77

$$\oint_{\partial\Omega} (\nabla\psi) \cdot d\mathbf{s} = 0. \quad (79)$$

Thus, choosing an arbitrary zero-point $\mathbf{0}$ on the shield, for any point \mathbf{R} on the surface of the shield we set

$$\psi(\mathbf{R}) = \int_{\mathbf{0}}^{\mathbf{R}} \mathbf{B}_I \cdot d\mathbf{s}. \quad (80)$$

We thus have a relation between the scalar potential $\psi(\mathbf{R})$ on the shield surface, and the induced magnetization \mathbf{B}_I at any position inside the vapor cell.

Following now the same reasoning as in sec.3.2 we exploit the fact that there are infinitely many solutions for $\psi(\mathbf{R})$ giving the desired magnetic field at the target points, and hence subject an optimization that minimizes the three dimensional Laplacian according to eq.73.

In case we choose to incorporate this into the script that calculates the PCB traces, we may, as may the interested reader, find guidance in [28].

B PCB Traces

Here we show the traces that were used to produce the three pairs of bias-coils. The thin black lines indicate the boundaries of the PCBs and the thick black line show the copper traces.

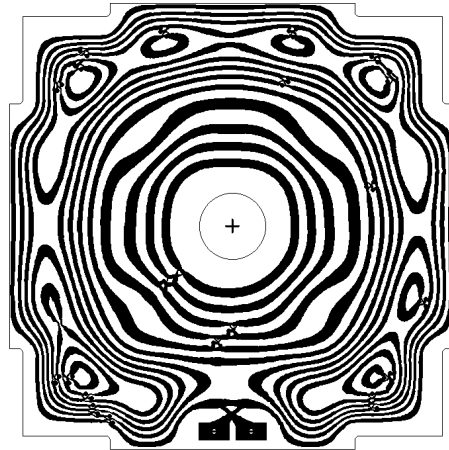


Figure 48: The final traces for the x -coils. The two squares in the bottom indicate the in -and outgoing currents. In the center is a hole enabling the probe beam to propagate freely.

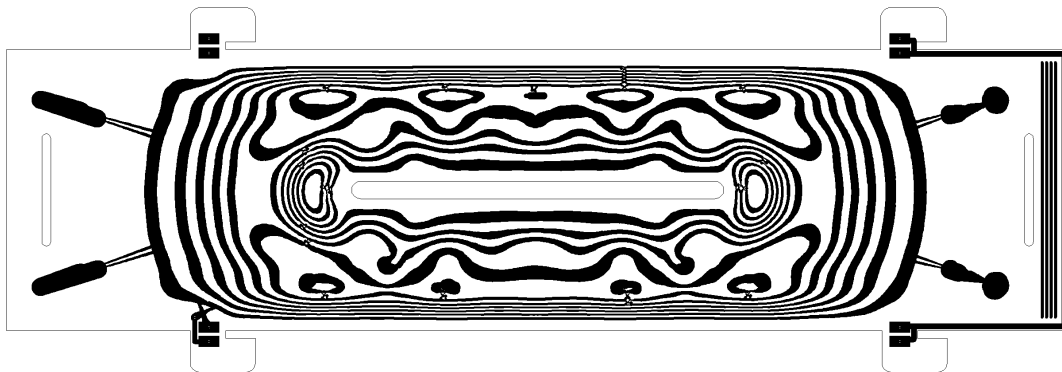


Figure 49: An illustration of the traces used to produce the y -bias coils. The two squares in the bottom left indicate the in -and outgoing current. Along the edge on the right side is a trace to take current from one z -bias coil to the other, and back. In the center is an elongated slit through which the pumping beams can propagate.

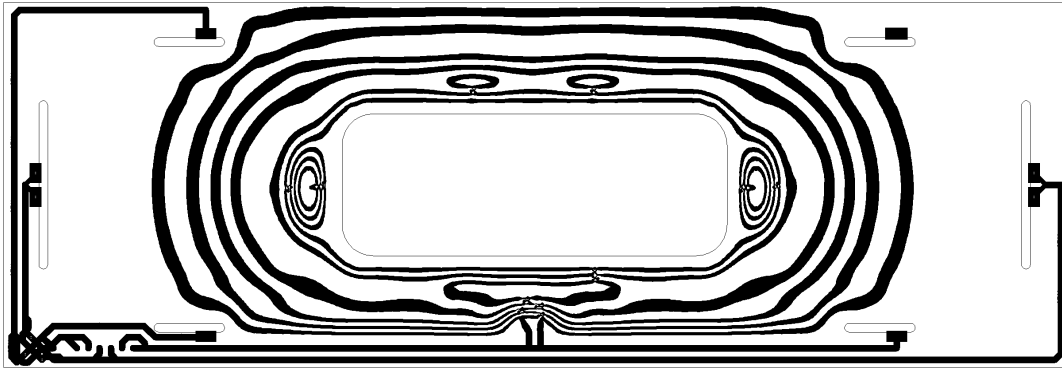


Figure 50: The final traces used for the z -bias coils. In the bottom left is a HUB to which all current supplies are connected and then distributed to the other PCBs. In the center is a big hole to make room for the stem of the vapor cell seen in fig.31.

C GWD-Lab Setup

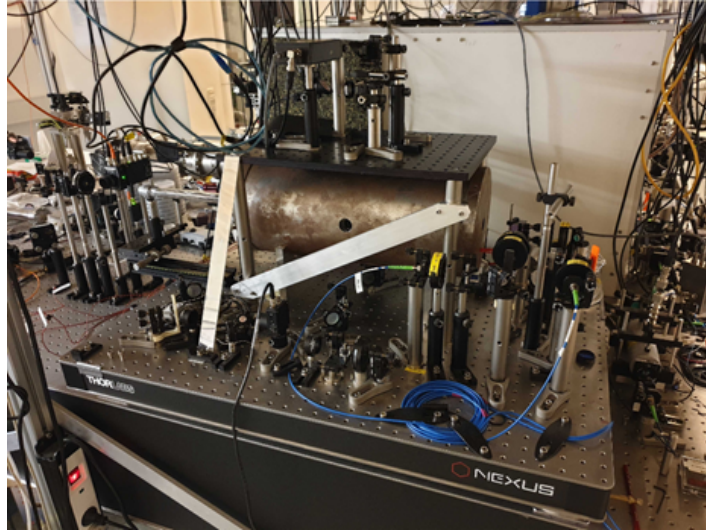


Figure 51: The setup of the magnetic shield and the corresponding optics in the GWD-lab.

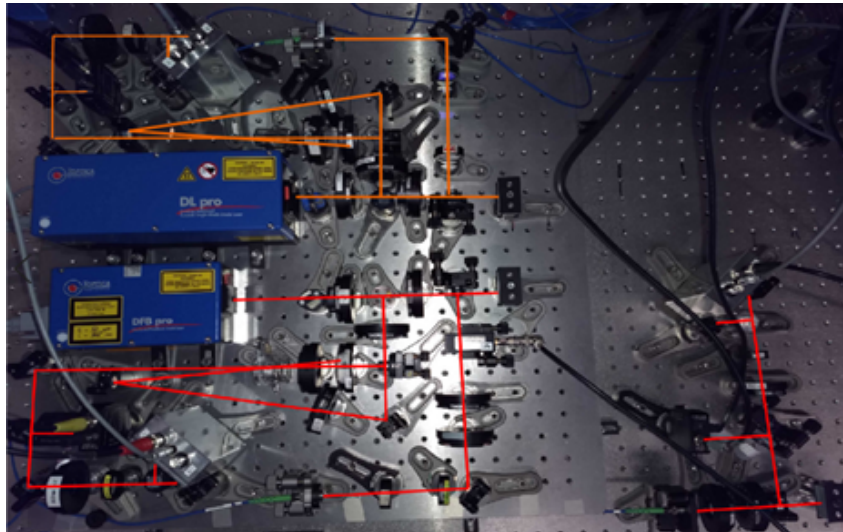


Figure 52: The two lasers used in MORS measurements conducted in the GWD-lab.



Figure 53: A picture of the inside of the magnetic shield where both the coil system and the 8 cm cell is mounted.

D Gravitational Waves

The derivation of gravitational waves is inspired by [14]. We remind ourselves of Einsteins equations

$$R_{\mu\nu} - \frac{1}{2}g_{\mu\nu}R = 8\pi GT_{\mu\nu} \quad (81)$$

where $R_{\mu\nu}$ is the Ricci tensor, $g_{\mu\nu}$ the metric, R the Ricci scalar, G the gravitational constant and $T_{\mu\nu}$ the energy-momentum tensor.

In the limit of weak gravitational fields the metric may be written

$$g_{\mu\nu}(x) = \eta_{\mu\nu} + h_{\mu\nu}(x) \quad (82)$$

where $h_{\mu\nu}(x)$ is the contribution from the gravitational field with the requirement $|h_{\mu\nu}(x)| \ll 1$, and $\eta_{\mu\nu}$ is the Minkowski metric

$$\eta = \begin{pmatrix} -1 & 0 & 0 & 0 \\ 0 & 1 & 0 & 0 \\ 0 & 0 & 1 & 0 \\ 0 & 0 & 0 & 1 \end{pmatrix}. \quad (83)$$

The general form of the invariant line-element ds is

$$ds^2 = g_{\mu\nu}dx^\mu dx^\nu \quad (84)$$

which, in Minkowski space, is given by

$$ds^2 = -dt^2 + (dx^1)^2 + (dx^2)^2 + (dx^3)^2. \quad (85)$$

The geodesic equation describing the motion of freely falling objects is in general given by

$$\frac{d^2x^\mu}{d\tau^2} + \Gamma_{\nu\rho}^\mu \frac{dx^\nu}{d\tau} \frac{dx^\rho}{d\tau} = 0 \quad (86)$$

where $\Gamma_{\nu\rho}^\mu$ is the Christoffel symbol which, in the case of the metric in eq.82 becomes

$$\Gamma_{\mu\nu}^\rho = \frac{1}{2} (\partial_\mu h_\nu^\rho + \partial_\nu h_\mu^\rho - \partial^\rho h_{\mu\nu}). \quad (87)$$

Combining eqs.86 and 87 we get the linearized geodesic equation in the weak field limit

$$\frac{d^2x^\rho}{d\tau^2} = - \left(\partial_\mu h_\nu^\rho - \frac{1}{2} \partial^\rho h_{\mu\nu} \right) \frac{dx^\mu}{d\tau} \frac{dx^\nu}{d\tau}. \quad (88)$$

By applying a Lorenz gauge for $h_{\mu\nu}(x)$ that obeys

$$\partial^\mu \left(h_{\mu\nu} - \frac{1}{2} \eta_{\mu\nu} h^\rho_\rho \right) = 0 \quad (89)$$

one can obtain the linearized Einstein equations

$$\square h_{\mu\nu} = -16\pi G \left(T_{\mu\nu} - \frac{1}{2} \eta_{\mu\nu} \eta^{\mu\nu} T_{\rho\sigma} \right) \quad (90)$$

where $\square = \eta^{\mu\nu} \partial_\mu \partial_\nu = \partial_\mu \partial^\mu$ is known as the d'Alembert operator.

In vacuum $\square h_{\mu\nu} = 0$ and in this case eq.90 is known as the relativistic wave equation. Make now the ansatz

$$h_{\mu\nu}(x) = A_{\mu\nu} e^{ik_\rho x^\rho} \quad (91)$$

where k is the 4-dimensional wave vector. If $k_\mu k^\mu = 0$ then eq.91 are solutions to eq.90 corresponding to monochromatic plane waves with $v = c$, that is propagating at the speed of light.

As for the polarization of this plane wave, since $A_{\mu\nu}$ is a 4×4 matrix, it initially has 16 (independent) entries. However, by making certain assumptions, such like symmetry, together with requiring that the conditions of a particular Lorenz gauge transformation are met, this can be reduced to just 2 physically distinct components - or independent polarizations. To summarize, the requirements are

$$k_\mu k^\mu = 0 \quad , \quad A_{\mu\nu} = A_{\nu\mu} \quad , \quad k^\mu A_{\mu\nu} = 0 \quad , \quad A_{\mu 0} = 0 \quad , \quad \eta^{\mu\nu} A_{\mu\nu} = 0. \quad (92)$$

Assume now a gravitational wave with frequency ω propagating along x^3 . Then $k^\mu = (\omega, 0, 0, \omega)$ and by imposing eqs.92 we can write

$$A_{\mu\nu} = \begin{pmatrix} 0 & 0 & 0 & 0 \\ 0 & A_{11} & A_{12} & 0 \\ 0 & A_{12} & -A_{11} & 0 \\ 0 & 0 & 0 & 0 \end{pmatrix}. \quad (93)$$

Write now the entries in complex form

$$A_{11} = B_1 e^{i\psi_1} \quad , \quad A_{12} = B_2 e^{i\psi_2}. \quad (94)$$

Then

$$\begin{aligned} h_{11} &= -h_{22} = B_1 \cos(\omega(x^3 - t) + \psi_1) \\ h_{12} &= h_{21} = B_2 \cos(\omega(x^3 - t) + \psi_2) \end{aligned} \quad (95)$$

is the only non-zero components of $h_{\mu\nu}$.

The line-element in eq.84 thus becomes

$$ds^2 = -dt^2 + (1 + h_{11})(dx^1)^2 + 2h_{12}dx^1 dx^2 + (1 - h_{11})(dx^2)^2 + (dx^3)^2. \quad (96)$$

We are now interested in exploring the relative motion between two test-particles. Consider a gravitational wave obeying eqs.95 and 96. Any particle following

$$x^0 = \tau \quad x^i = \text{const.} \quad (97)$$

would then be on what is known as a time-like geodesic ($v < c$). The meaning of eq.97 is that we place a particle in a (spatial) position and only the time-coordinate changes. Say now that we have two such particles, A and B , with the spacial coordinates

$$\begin{aligned} x_A &= (x_A^1, x_A^2, x_A^3) \\ x_B &= (x_1^A + L_0 \cos \theta, x_A^2 + L_0 \sin \theta, x_A^3) \end{aligned} \quad (98)$$

where both particles have purposely been chosen to lie within a plane perpendicular to the axis of propagation of the gravitational wave. An illustration is seen in fig.54.

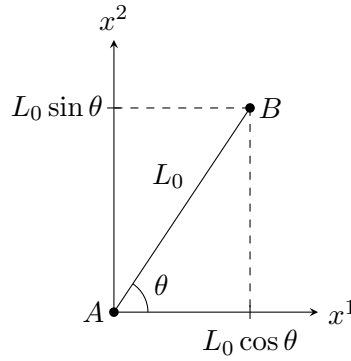


Figure 54: An illustration of the positions of the two test-particles A and B .

From eq.96 one can now calculate the length L between these two particles to find

$$L(t) = \left[1 + \frac{1}{2} h_{11}(t) \cos(2\theta) + \frac{1}{2} h_{12}(t) \sin(2\theta) \right] L_0. \quad (99)$$

We see that the length L is time-dependent through $h_{\mu\nu}$. It is this relative motion of test-particles that makes it possible to detect gravitational waves. Note also that, since $\cos(2\theta) = \sin(2(\theta + \pi/4))$, the effect on L from h_{11} compared to that of h_{12} is rotated 45 degrees. Hence they are linearly independent.

Let us now examine a grid of test-particles in the x^1, x^2 -plane. Let $B_2 = 0$ in eq.95. Then eq.99 becomes

$$L(t) = L_0 \left[\frac{1}{2} B_1 \cos(\omega t) \cos(2\theta) \right]. \quad (100)$$

For a pair of particles lying along x^1 where $\theta = 0$ we have $\cos(2\theta) = 1$. For another pair lying along x^2 where $\theta = \pi/2$, we get $\cos(2\theta) = -1$. This means that the lengths between these two pairs of particles respectively oscillate out of phase.